Rohdenburg, Markus ; Winkler, Robert ; Kuhness, David ; Plank, Harald ; Swiderek, Petra

Water-Assisted Process for Purification of Ruthenium Nanomaterial Fabricated by Electron Beam Induced Deposition

Journal Article	as:	peer-reviewed accepted version (Postprint)
DOI of this document*(secondary publication):		https://doi.org/10.26092/elib/3710
Publication date of this document:		19/02/2025

* for better findability or for reliable citation

Recommended Citation (primary publication/Version of Record) incl. DOI:

Water-Assisted Process for Purification of Ruthenium Nanomaterial Fabricated by Electron Beam Induced Deposition. Markus Rohdenburg, Robert Winkler, David Kuhness, Harald Plank, and Petra Swiderek
ACS Applied Nano Materials 2020 3 (8), 8352-8364
DOI: 10.1021/acsanm.0c01759

Water-Assisted Process for Purification of Ruthenium Nanomaterial Fabricated by Electron Beam-Induced Deposition (EBID)

Markus Rohdenburg,[a]* Robert Winkler,[b] David Kuhness,[b] Harald Plank[b,c,d] and Petra Swiderek[a]*

a *University of Bremen, Institute of Applied and Physical Chemistry, Fachbereich 2 (Chemie/Biologie), Leobener Straße / NW 2, Postfach 330440, D-28334 Bremen, Germany*

b *Christian Doppler Laboratory for Direct–Write Fabrication of 3D Nano–Probes (DEFINE), Institute of Electron Microscopy and Nanoanalysis, Graz University of Technology, Steyrergasse 17, A-8010 Graz, Austria*

c *Institute of Electron Microscopy and Nanoanalysis, Graz University of Technology, Steyrergasse 17, A-8010 Graz, Austria*

d *Graz Centre for Electron Microscopy, Steyrergasse 17, A-8010 Graz, Austria*

*Corresponding author emails: m.rohdenburg@uni-bremen.de (M.R.), swiderek@uni-bremen.de (P.S.)

Abstract

The purity of nanomaterials fabricated by focused electron beam induced deposition (FEBID) is often not high enough for the desired application. For instance, large amounts of carbon incorporated into the deposits deteriorate their electrical conductivity. Such impurities stem from incomplete electron-induced fragmentation of the applied precursors. Except for nanomaterials containing the most noble and thus oxidation-resistant metals, deposits cannot be purified by harsh post-processing steps like O_2 treatment and excessive thermal annealing is detrimental to the desired shape fidelity. Milder purification protocols based on electron irradiation in presence of H_2O vapor have thus been developed and it was demonstrated that they yield pure Pt and Au deposits. Herein, we report on the application of such a water-assisted purification strategy to deposits produced from the FEBID precursor bis(ethylcyclopentadienyl)ruthenium(II) ($(EtCp)_2Ru$). Such Ru nanomaterials are relevant to the repair of masks for extreme ultraviolet lithography. In contrast to noble metals, where higher doses lead to higher purity, and contrary to purification using O_2 that is accompanied by a continuous increase of the oxygen content, we here demonstrate the existence of an ideal purification dose for Ru-based FEBID materials, where oxidation is kept at a minimum while carbon is effectively removed from the deposits. In addition, a complementary surface study under ultrahigh vacuum conditions provides insight in the chemistry that transforms the carbonaceous contamination to CO. The results provide evidence that water-assisted purification can be applied to a wider range of FEBID deposits also including those containing Ru as an example of a less noble metal.

Keywords

Focused electron beam induced deposition, ruthenium nanostructures, deposit purification, carbon removal, water-assisted process, electron-induced chemistry, surface science study

1. Introduction

Focused Electron Beam Induced Deposition (FEBID) is a direct-write technique to fabricate nanostructures by decomposing suitable precursor molecules under the well-focused high energy electron beam of an electron microscope.[1-5] For FEBID of metallic structures, organometallic precursors are employed. These must fulfil several requirements, the most important being (i) sufficient volatility to allow dosing of the precursor *via* the gas phase and (ii) low stability under electron exposure to enable complete removal of the organic components of the precursor. Extensive research has addressed the search for an "ideal" FEBID precursor that exhibits both properties and many candidates have already been studied.[1-7] Also, a substantial catalogue of precursors tailored for Chemical Vapor Deposition (CVD)[8] or Atomic Layer Deposition (ALD)[9,10] processes relying on thermal chemistry is readily available. Unfortunately, however, volatility and fragility under electron exposure do not necessarily go hand in hand. Contrariwise, precursor molecules containing large organic ligands are often highly volatile but their organic ligands tend to be difficult to remove by mere electron irradiation.[1,11] Unwanted side reactions such as oligomerization are likely to occur.[12] Carbon-free precursors, on the other hand, avoid carbonaceous contamination on the surface but often exhibit insufficient vapor pressure or lead to inorganic residues in the deposit.[13,14]

Although carbonaceous FEBID deposits have applications such as humidity[15] or strain[16] sensing, high purity materials are essential for most applications in which, for instance, electrical conductivity is required. Hence, substantial effort has been made to increase deposit purity by applying external stimuli to the as-deposited FEBID structures such as prolonged electron exposure,[17] thermal treatment[18] or the application of process gases like oxygen which can remove carbon contaminations by oxidation.[19-21] Recently, H_2O vapour has been applied as a particularly successful purification agent under prolonged electron irradiation as proven for highly contaminated deposits produced from trimethyl(methylcyclopentadienyl)platinum(IV) ($MeCpPtMe_3$),[22] a widely applied FEBID precursor for Pt deposition with favourable vapor pressure. Unfortunately, $MeCpPtMe_3$ leads to incorporation of extensive amounts of carbon in the deposits. However, it was shown that pure and densely-packed Pt deposits can be obtained by water-assisted purification and their shapes remained stable throughout the

purification procedure.[22] The same procedure was successfully applied to 2D as well as for freestanding 3D FEBID materials produced from $Me_2Au(acac)$, resulting in plasmonically active nanostructures.[23] In a similar purification approach, simultaneous dosing of $Me_2Au(tfac)$ and H_2O during FEBID also resulted in deposits with high Au content.[24]

Herein, we demonstrate that a water-assisted post-deposition purification protocol can be applied to FEBID deposits produced from the Ru precursor bis(ethylcyclopentadienyl)ruthenium(II) ($(EtCp)_2Ru$, Figure 1). $(EtCp)_2Ru$ has been considered before as an appropriate precursor for deposition of ruthenium(IV) oxide (RuO_2) and even pure ruthenium by FEBID[25] being highly relevant as thin Ru or RuO_2 capping layers in the context of Extreme Ultraviolet lithography (EUVL).[26-30] In brief, EUVL mask repair of Ru-based capping layers *via* FEBID calls for processes, which produce material with a very low carbon content. We note that, as an alternative to $(EtCp)_2Ru$, η^3-allyl ruthenium tricarbonyl halides $[(\eta^3\text{-}C_3H_5)Ru(CO)_3X]$ (X = Cl, Br) and have been proposed as a novel class of Ru precursors.[31-35] Very recently, also $Ru(CO)_4I_2$ was brought forward as a precursor for electron-induced deposition of Ru material with low carbon content.[36] Electron irradiation efficiently removes CO from these compounds resulting in a lower amount of carbon residues in the deposit but at the cost of halide contamination that can only be reduced by extensive electron exposures.[32] Therefore, the use of $(EtCp)_2Ru$ as a FEBID precursor for Ru deposition is still of fundamental interest given that suitable processing conditions can be identified that yield carbon-free Ru deposits with high-fidelity morphologies within conveniently applicable timeframes. Noh et al. demonstrated carbon removal from $(EtCp)_2Ru$ deposits with an initial elemental ratio of RuC_9 by the aid of O_2 as purifying agent, while typical morphological disruption by means of pinhole- / crack-formation could be reduced by lowering the temperature of the reactive gas down to 25 °C.[25] In contrast, the application of room temperature H_2O as reactive gas has been demonstrated to be much more suited[22-24] due to high purification efficiencies, minor implications on the morphology and comparably simple technical implementation *via* environmental scanning electron microscopes (ESEM). Together with the proven ability of H_2O to prevent oxidation during Ru ALD,[37] water assisted electron beam purification is a highly promising concept towards pure, FEBID based Ru materials as borderline representative between noble and transition metals, that readily dissociate H_2O and tend to form oxides.[38]

Based on that motivation, this study focuses on the evolution during post-growth purification of FEBID structures fabricated from $(EtCp)_2Ru$. The purification process is explored *via* morphological, chemical and structural analyses and complemented by surface science experiments performed under ultrahigh vacuum (UHV) conditions. The study starts with dose dependent volume-loss measurements *via* atomic force microscopy (AFM) followed by chemical analyses using electron-based energy-dispersive X-ray spectroscopy (EDX) by *in situ* and *ex situ* measurements and imaging of structural details *via* transmission electron microscopy (TEM). In the second part, the study employs surface science model experiments, that monitor deposition and purification in highly pure environments to reduce unwanted reactions to the technically possible minimum. By using a previously validated approach for FEBID materials,[39] volatile products evolving from the deposit under electron irradiation and thermal treatment are monitored by mass spectrometry (MS), while the progress of deposit purification can be deduced from Auger electron spectroscopy (AES). The study reveals two electron driven processes in H_2O environments, whose balance changes with the applied dose. While *carbon removal* initially dominates, *oxidation* sets in at very low carbon contents, revealing that careful dosing during purification enables the fabrication of Ru materials with low carbon content and, at the same time, minimal degree of oxidation. This is in clear contrast to the earlier O_2-based process for carbon removal that is accompanied by a continuous increase in the oxygen content of the deposit.[25] The experimental results are complemented by a model to explain the chemical reactions during H_2O assisted electron beam purification of $(EtCp)_2Ru$ based FEBID materials.

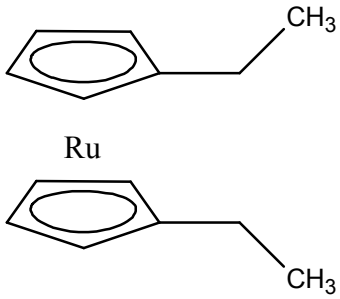

Figure 1. Molecular structure of bis(ethylcyclopentadienyl)ruthenium(II) $(EtCp)_2Ru$.

2. Experimental section

2.1. Precursor

$(EtCp)_2Ru$ was purchased from STREM Chemicals in a stated purity of 98% (99.9% Ru) and was used without further purification. For each FEBID experiment, the precursor was freshly filled into the Gas Injection System (GIS) and stored at -20° C in between different days of deposition.

For the surface studies, the precursor was degassed by repeated freeze-pump-thaw cycles and kept under vacuum throughout all experiments.

2.2. FEBID, water-assisted purification and deposit analysis

Fabrication. 500 x 500 nm² pads were deposited in a FEI Quanta 3D FEG (FEI Company, The Netherlands) dual beam microscope (DBM) on Si substrates (with 3 nm thermal SiO_2)[22] using the $(EtCp)_2Ru$ precursor. The DBM consists of an ESEM and a focused ion beam (FIB) microscope. For deposition, the standard FEI GIS was employed with the nozzle placed in a vertical distance of 100 µm to the substrate at an angle of 52°, 25 µm off-axis and a projected distance to the beam centre of 110 µm. The GIS temperature was set to 50°C in accordance to the literature procedure[25] and deposition was carried out at a pressure of approximately 1.6×10^{-6} mbar (base pressure: 9.5×10^{-7} mbar). For deposition, a serpentine scan strategy was chosen with a primary beam energy of 5 keV, a beam current of 58 pA, 10 µs dwell time (DT) and 13 nm point pitch (PoP). This choice of parameters is in accordance to optimized conditions with respect to surface morphology as reported in reference.[40] The thickness of the deposited pads was controlled by varying the number of passes.

Purification. Purification was performed *in situ* in the DBM in low pressure (LP) mode at a H_2O partial pressure of 50 Pa. RuC_9[25] pads were purified with a primary beam energy of 5 keV, a beam current of 5.6 nA, 1 µs DT and 4 nm PoP in accordance with successful purification conditions as applied to deposits made from $MeCpPtMe_3$.[22] The purification frames of 2000 x 2000 nm² were centred on the 500 x 500 nm² deposits. The beam current under the present conditions was determined with a Faraday cup.

Characterization. AFM measurements were conducted with a FastScan Bio AFM microscope in tapping mode employing AFM tips with spring constants of 17 N/m (FASTSCAN-A, Bruker NANO,

CA, USA) in soft repulsive conditions. Analyses were done with the software packages Nanoscope Analysis 1.8 (Bruker NANO, CA, USA) and Gwyddion 2.53. To provide comparability of surface roughness, analyses was always performed across 252 x 252 nm² areas in the centre of each pad, which excludes deposition regime related morphology effects at edges and corners.[40] EDX was performed at a beam energy of 5 keV either *in situ* with an EDAX XL-30 EDX system (EDAX, USA) installed at the DBM (high vacuum (HV) conditions) and a beam current of 20 nA, or *ex situ* with an EDAX Element EDS System (EDAX, USA) on a Quanta 600 FEG ESEM microscope (FEI Company, The Netherlands) with a beam current of 0.6 nA. For dose dependent analyses, we always integrated the counts for the following ranges to derive individual intensities: (low energy range, L) 0.14-0.34 keV (C and Ru overlapping), (medium energy range, M) 0.36-0.60 keV (O) and (high energy range, H) 2.4-3.2 keV (Ru). A sputter-cleaned Ru standard (ASTIMEX Scientific Limited; 99,9% wire Goodfellow Inc., UK) was used as reference sample.

Transmission Electron Microscopy. For transmission electron microscopy (TEM) characterization, $(EtCp)_2Ru$ deposits were fabricated with initial heights of 85 nm on the same Si substrates using the above described general parameters for deposition and purification. Purification was executed with doses of 6 C/cm², 12 C/cm² and 30 C/cm². The purified deposits were then covered with a FEBID based Pt-C protection layer ($MeCpPtMe_3$ precursor in the as deposited state) and subjected to a careful lamella preparation *via* Ga^+ FIB standard protocols. As oxidation at lamella surfaces is unavoidable during DBM-TEM transfer, the lamellas were not thinned below 80 nm to keep surface-to-volume ratio low. After DBM-TEM transfer the samples were immediately characterized by a FEI Tecnai TF 20 (FEI Company, The Netherlands), equipped with a Schottky emitter operated at 200 kV. Image analyses were performed *via* the software package Digital Micrograph GMS 3 and ImageJ 1.52p.

2.3. Surface study under UHV conditions

Surface model studies on the electron-induced decomposition of $(EtCp)_2Ru$ and deposit purification were carried out in a UHV apparatus operated at a base pressure of approximately 10^{-10} mbar.[39] The setup consists of two chambers between which a polycrystalline Ta sheet can be translated. This substrate with a total area of 5 cm² exposed to the electron beam is mounted on a copper sample holder

attached to a liquid N_2 bath cryostat, allowing for cooling to about 110 K. The bottom chamber contains a quadrupole mass spectrometer (QMS, SRS RGA 300) and a commercial flood gun (SPECS FG 15/40) for electron exposure arranged at an angle of 60° with respect to each other and 30° with respect to the substrate. The electron gun generates an electron beam with adjustable energy (E_0 = 1-500 eV) and an energy resolution in the range of 0.5-1 eV with current densities set in the range 10-30 μA/cm². Furthermore, a stainless-steel capillary pointing towards the substrate is connected to a gas handling manifold from which vapours can be introduced to the chamber. The top chamber contains an AES (Staib DESA 100 equipped with a high-energy electron gun and a cylindrical mirror analyser (CMA)) to monitor the condition of the substrate in terms of elemental composition and an ion gun utilized to sputter-clean the substrate before each experiment with Ar^+ ions at an incident energy of 3 keV. The substrate was considered to be ready for a new experiment when the Ta signals were clearly visible in AES. Moreover, volatile residues adsorbed on the substrate were removed by annealing to 450 K which was conducted using resistive heating through two thin Ta ribbons spot-welded to the Ta sheet.

Adsorption of $(EtCp)_2Ru$ and H_2O on the substrate was achieved by leaking substance vapour from the calibrated volume of a gas handling manifold to the cooled Ta sheet. The amount of substance that was dosed was monitored as the pressure drop in the manifold upon leaking as measured by a capacitance manometer. The thickness of the adsorbed precursor layer was estimated by dosing amounts of vapor corresponding to different pressure drops in the gas handling manifold and subsequently performing a thermal desorption experiment (see below). The integral of the precursor's desorption signal (Supporting Information, Figure S1) is proportional to the amount of substance on the substrate. As a result, the transition from monolayer to multilayer coverage for $(EtCp)_2Ru$ occurred in the pressure drop range 0.20-0.30 mTorr. Precursor doses used in the experiments corresponded to a pressure drop of 4.0 mTorr, so that the film thickness can be estimated as 13-20 monolayers (ML).

Desorption experiments, i.e. electron-stimulated desorption (ESD), thermal desorption spectrometry (TDS) and isothermal desorption spectrometry (IDS) were conducted using the QMS operated either in full mass scan mode or recording selected masses over time. TDS was performed by applying a constant temperature ramp of 1 K/s through resistive heating to the substrate while simultaneously monitoring

gas phase composition by QMS. ESD and IDS were conducted at constant temperature (110 K) with or without exposing the substrate to electrons, respectively, while recording mass spectra.

AES was typically performed at an excitation electron energy of 5 keV using pulse counting collection mode. Spectra were recorded under fixed retarding ratio (FRR) conditions at a variable energy resolution of dE/E = 0.6%. Typical beam currents were in the order of 2-3 μA. The obtained AE spectra were subjected to a baseline correction employing an Asymmetric Least Squares Smoothing (ALS) algorithm and subsequently the first derivative dN/dE with respect to the kinetic energy was numerically calculated and afterwards smoothed by a Savitzky-Golay filter of 9 eV bandwidth. Quantification was performed employing Peak-to-Peak (PtP) heights which were corrected for the specific sensitivity factors of relevant elements.[41]

3. Results and discussion

3.1. FEBID, water-assisted purification, and deposit analysis

3.1.1. Deposit formation

$(EtCp)_2Ru$ deposits were fabricated with 5 keV/58 pA (see Section 2.2. for patterning details) with a deposit footprint area of 500×500 nm^2. AFM assisted pre-experiments revealed ***i)*** a nearly linear height increase with the number of passes (Supporting Information, Figure S2) and ***ii)*** a high reproducibility, as reflected by less than 1 nm height variation for 25 produced square deposits with a target height of 50 nm (Supporting Information, Figure S3). Unless otherwise stated, we chose a target height of 120 nm for all deposits. The actual thickness of individual samples was determined from AFM data as reported below.

3.1.2. Deposit purification

Ruthenium has a higher susceptibility towards reaction with H_2O or oxygen than e.g. Pt or Au.[38] Therefore and in contrast to our previous studies on deposits made from $MeCpPtMe_3$[22] and $Me_2Au(acac)$,[23] the water-assisted purification of deposits fabricated from $(EtCp)_2Ru$ was studied *in situ*, i.e., without exposing the deposits to ambient conditions in between deposition and purification. This novel *in situ* purification procedure is enabled by a microscope with low pressure (LP) capability and excludes any uncontrolled contribution of atmospheric O_2. Furthermore, we compare the results obtained by this novel procedure to a sample purified by the established *ex situ* purification protocol involving sample transfer between FIB and ESEM microscope under ambient conditions.[22] This allows us to evaluate the sensitivity of the deposits produced from $(EtCp)_2Ru$ towards handling in air.

Morphology and Shape Fidelity. The choice of purification parameters was guided by previous water-assisted purification experiments.[22] The beam energy was fixed to 5 keV to enable sufficient penetration of the 120 nm thick deposits, prerequisite to achieve full purification (see simulations in Supporting Information, Figure S4 and S5). The beam current was set to 5.6 nA without further adaption as purification rates were found to be high, while surface morphologies were not disrupted at all (details see later).[22] The H_2O partial pressure was fixed to 50 Pa since for purification of deposits from $MeCpPtMe_3$[22] and $Me_2Au(acac)$,[23] the morphological and compositional results were widely independent of the H_2O pressure in a range of 10-100 Pa, indicative of a process rather limited by electron flux than mass transport.[22] The purification dose was then systematically varied between 1 and 200 C/cm², while morphological and chemical implications were studied.

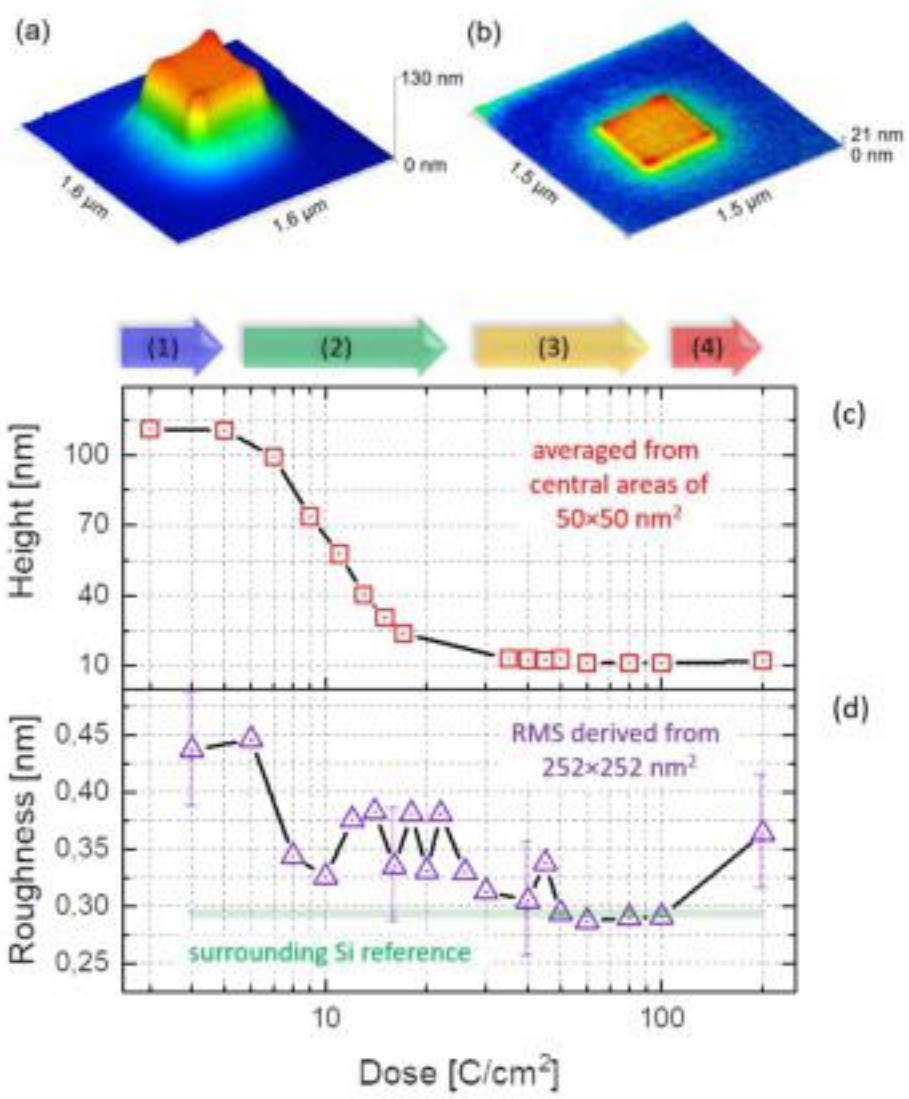

Figure 2. (a) and (b) show 3D AFM height images of a Ru based FEBID deposit before and after a 100 C/cm² purification, respectively. While vertical scaling is identical for direct comparison, colors were adjusted to visualize relevant surface details and in particular the crack-free shape fidelity. (c) and (d) show the dose dependent evolution of deposit heights and RMS surface roughness, respectively. Both quantitites are derived from central deposit areas as specified within the graphs. Note the logarithmic abscissa (dose) to reveal the ealy stage behavior. For clarity, only four error bars are shown in (d). Discussion and interpretation can be found in the main text.

Figure 2 shows an AFM based, in-scale comparison of a 500×500 nm² deposit before (a) and after purification with a dose of 100 C/cm² (b). All deposits revealed concave top morphologies as consequence of the local working regime.[40] Thus, height values were averaged from 50×50 nm² wide regions at the center. We also want to mention the distinct proximity deposition outside the intended

500×500 nm² footprint (confirmed *via* cross-sectional TEM), which mainly originates from substrate-related backscattered electrons.[42] Figure 2(c) shows the typical dose dependent height decrease, which reveals four different stages as indicated on top: (1) no height losses up to about 5 C/cm², (2) fast height loss down to about 25% of the initial height after 10–20 C/cm², (3) slow additional height loss down to 10% after ~100 C/cm² and (4) weak height increase for doses > 100 C/cm². At this point it is essential to mention that volume losses mainly proceeded *via* height loss instead of lateral shrinkage which is always less than 1% of the structure size. Beside the advantage of footprint retention, this purification approach was demonstrated to qualitatively maintain 3D shapes, while surfaces were found to be crack- and pore-free during AFM analyses.[22,23] To evaluate whether that also holds for $(EtCp)_2Ru$ based FEBID deposits, high-resolution AFM was conducted on differently purified deposits. Figure 2(d) summarizes the dose-dependent RMS roughness evolution, taken from of 252×252 nm² wide areas in the deposit center. As evident, there are also 4 stages in good agreement with the height loss: (1) constant RMS roughness and deposit height, (2) fast decrease, (3) slow decrease and (4) slow increase. We note that the slightly increasing values between 10 C/cm² and 40 C/cm² must be taken with caution when considering the four representative error bars. Also, the absolute values should be kept in mind, which indicate nanometer smooth surfaces without pores or cracks, as further substantiated by high-resolution SEM images (Supporting Information, Figure S6). The same AFM study also revealed that individual surface features, such as elevated edges and corners, are qualitatively well maintained (Supporting Information, Figure S7). The combined AFM results underline the morphology-preserving character of the H_2O-assisted electron beam purification as observed for Pt- and Au-based FEBID materials.

Chemical Composition. Figure 3(a) summarizes background corrected EDX spectra, which were acquired *in situ* in the same machine after different purification doses as specified in the figure caption. The shaded regions indicate characteristic peaks relating to Ru-Lα and Ru-Lβ (green), Si-Ka (grey) and O-Kα (blue). The red shaded region is of particular relevance as carbon's C-Kα and ruthenium's Ru-M edge overlap here. The latter is shown in detail in Figure 3(b), where the peak for as deposited materials (green) agrees with the expected carbon position, which reflects the high carbon content. During

purification, the intensity decays and reveals a shift of its maxima towards the expected Ru-M position (purple), while a C-Kα shoulder is barely recognizable. This clearly indicates the transfer from a C-dominated into a Ru-dominated material, representative of the intended carbon removal. Figure 3(c) and (d) also show individual spectra related to O and Ru with the Si-SiO_2 substrate spectra included as black dotted curves.

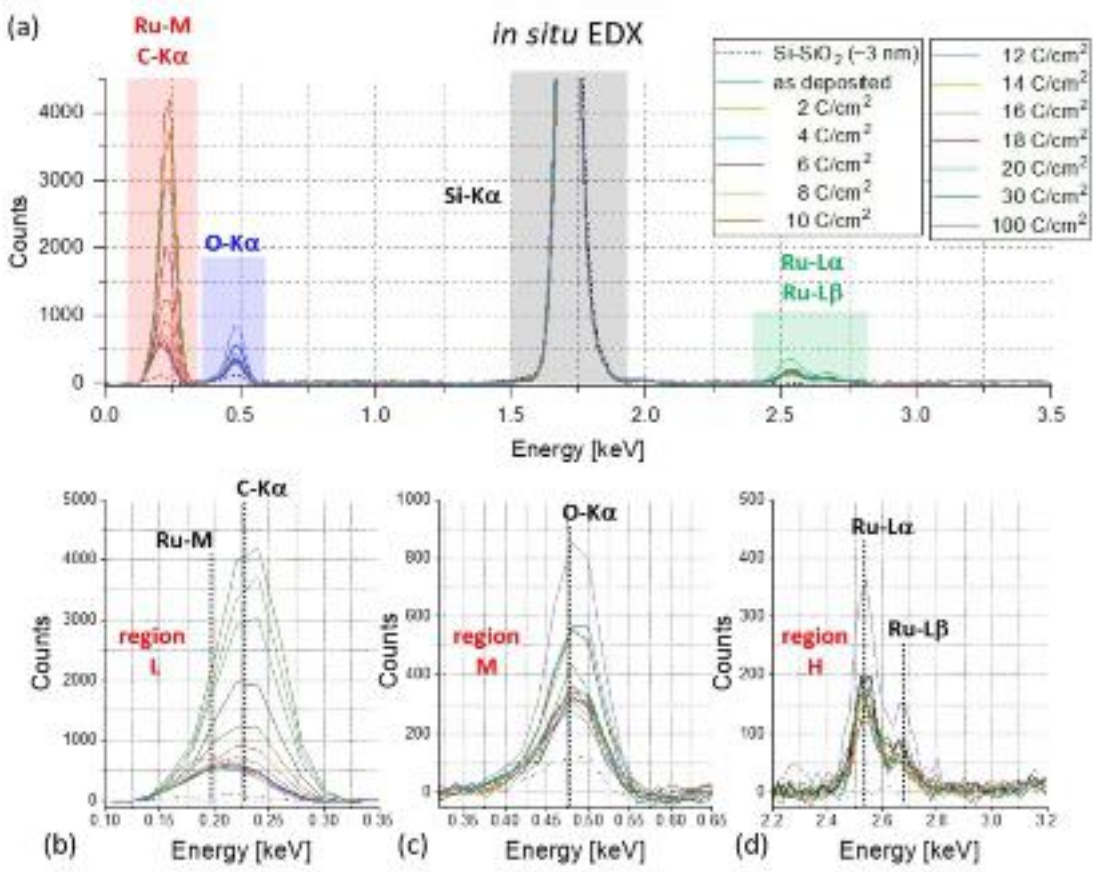

Figure 3. (a) *in situ* EDX spectra obtained after initial fabrication and different purification doses (see legend) without breaking the vacuum to exclude reactions with gases from the ambient. The shaded regions indicate characteristic peaks of different elements, which are shown in more detail in (b), (c) and (d), further denoted as region L, M and H, respectively.

A reliable quantification of light elements (C, O) *via* EDX is challenging, especially when measured on thin films, where X-rays are emitted from the substrate as well. The situation is even more complicated when relevant peaks are overlapping, which is the case here for carbon (C-Kα) and ruthenium (Ru-M), as indicated in Figure 3(b). We therefore follow our previous approach[22,23] by calculating background corrected integrated peak intensities as described in Section 2.2 for the convoluted *low energy range* as

shown in Figure 3(b) and relate that to the integrated peak intensity of the Ru *high energy range* shown in Figure 3(d), further denoted as ranges ***L*** and ***H***, respectively. As fully metallic reference, EDX was performed on sputter-cleaned Ru samples, which gives a L:H ratio of 1.02±0.1 (Supporting Information, Figure S8).

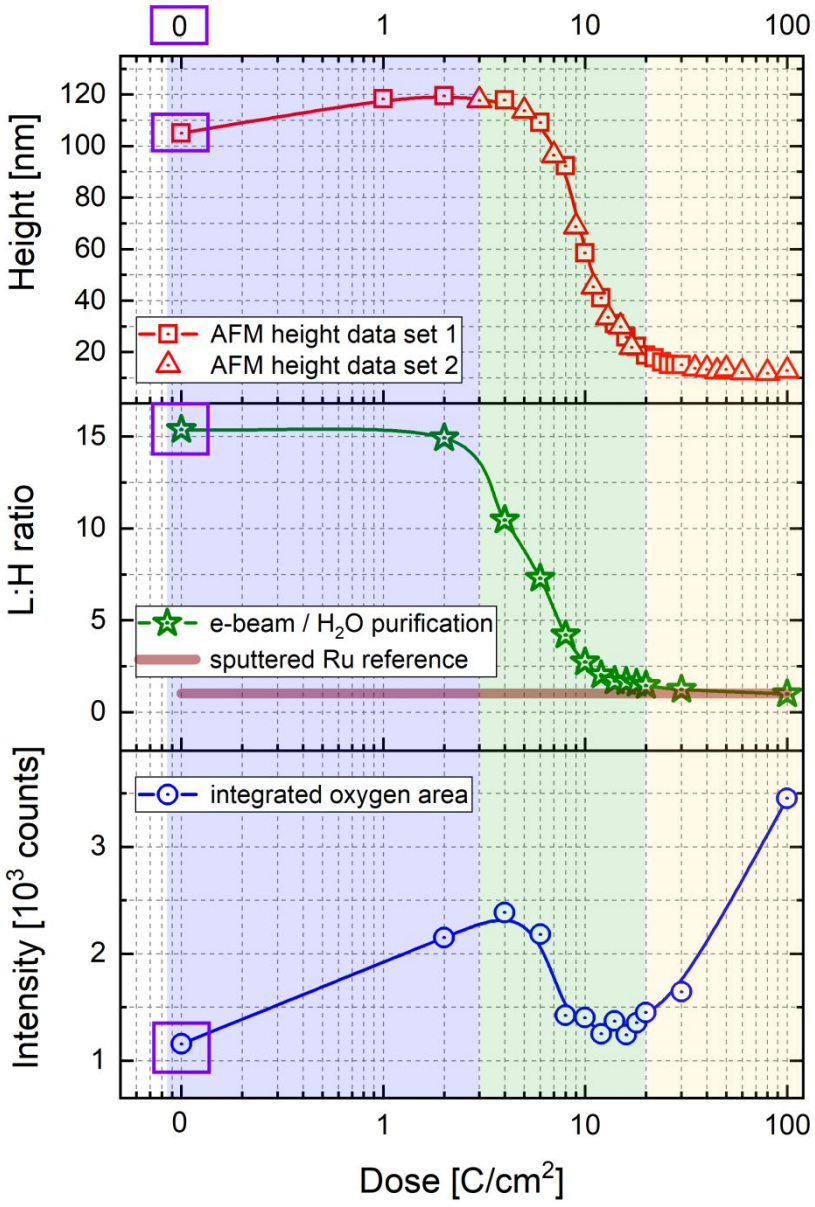

Figure 4. Dose dependent evolution of the deposit height for two data sets from different experiment measured by AFM (red squares / triangles, top panel), L:H intensity ratio as a measure for carbon removal (green stars, central panel) together with the Ru reference value from sputter-cleaned Ru samples (purple horizontal line, central panel), and oxygen intensity (blue circles, bottom panel). Note the logarithmic abscissa for the dose and that as-deposited values at the very left are emphasized by purple frames to visualize the evolution.

Figure 4 shows the L:H intensity ratio (center) along with the oxygen intensity (bottom) and the pad heights, the latter taken from two different experimental runs (see figure caption). The correlation suggests that purification proceeds in three phases, which agree well with phases (1)-(3) discussed in the morphology section above. In the first, blue-shaded phase up to 3–5 C/cm^2, we observe an increasing oxygen signal (bottom), which goes along with a slight height increase (~10%, top), while the L:H ratio as a measure for incorporated carbon remains nearly constant (center). Before an interpretation is given, we have to keep in mind, that after each dosing experiment, the deposits were brought back to high vacuum conditions for EDX measurement. Hence, the volume increase is unlikely to originate from incorporated water, as the high vacuum step would entirely "dry" the thin deposits. Therefore, we interpret the swelling as consequence of an irreversible electron induced reaction such as the formation of oxygenated intermediates (e.g. alcohols)[39] before the carbon matrix gets decomposed into volatile fragments (see Section 3.2). Such modification processes are likely to increase the matrix volume in agreement with the increasing heights, the stable carbon content, and the increasing amount of oxygen (bottom curve in Figure 4). We note that electron trajectory simulations exclude the 3 nm SiO_2 layer as origin of the oxygen increase during swelling (Supporting Information, Figure S9). In the second, green-shaded phase, effective carbon removal sets in, as clearly reflected by the decaying L:H intensity ratio (center) and the simultaneous volume loss (top). During that phase, the oxygen intensity also decays in agreement with the aforementioned decomposition into volatile carbon oxides CO_x (x = 1-2), as previously suggested[25] and directly observed in this study (see Section 3.2). At the end of this phase, the L:H intensity ratio approaches the Ru reference value of 1.02±0.1 (horizontal line), which indicates that the carbon removal is mostly completed (~10–20 C/cm^2). The L:H saturation entails a stagnation of the height loss at ~90% of the initial height and a distinct minimum in the oxygen intensities. This minimum is contrary to the earlier O_2-based purification process where a continuous increase in the oxygen content of the deposit was observed.[25] For higher doses (orange-shaded third phase), however, oxygen intensities rise again, while carbon content and deposit volume still decay at very low rates. Expanded experimental series with doubled final doses confirmed both, the continuous increase for oxygen and the weak decrease of the L:H ratio (Supporting Information, Figures S10 and S11). For highest doses, however, AFM data revealed a slight increase in volume and surface roughness, as evident in Figure 2.

Complementary TEM data confirmed that the inner granular structure is widely unchanged in the low dose region (phase 1), followed by gradual grain growth and / or coalescence in the carbon removal phase 2 until a densified layer is formed during phase 3 (see Supplementary Information, Figure S12). This behavior is in agreement with structural changes during this purification approach for Pt- and Au-based FEBID materials.[20,22,23,25,43-46] Unfortunately, TEM could not be used for reliable chemical analyses in this case, as the sub-100 nm thin Ru lamellae can oxidize in an uncontrolled manner during sample transfer from the DBM to the TEM under ambient conditions. We note that due to this problem, the direct proof of full oxygen removal is extremely complicated even if methods such as selected area electron diffraction (SAED) were applied. The FIB-assisted preparation of the lamellae also contributes to this difficulty because it induces heat and can bring oxygen from the SiO_2 substrate to the deposit. However, even a non-oxidizing substrate such as Au, beside posing problems related to overlapping EDX lines, would not solve the problem of having to differentiate between oxidation during the purification process and during subsequent transfer to the TEM.

The collective results from AFM, SEM, EDX and TEM allow the interpretation, that the electrons in the presence of low-pressure H_2O atmospheres trigger two competing chemical processes in deposits produced from $(EtCp)_2Ru$, namely carbon removal and oxidation. Although small, we observe deposit swelling for very low doses, which we propose to result from a chemical modification of the carbon matrix (see Section 3.2). Slightly after, matrix decomposition sets in and *electron-induced reactions lead to efficient carbon removal*. The structural evolution is very similar to those for Pt- and Au-based FEBID materials[22,23] and indicates a general decomposition mechanism as studied in detail in Section 3.2. Once most of the carbon is removed, the chemistry changes and the *oxidative processes between Ru and dissociated H_2O become dominant*. Here, we assume that oxidation takes place along the Ru grain boundaries within the nano-granular metal layer. Once the available space is fully consumed, ongoing oxidation leads to small increases of deposit heights and surface roughness. This two-process model is compatible with all available data presented so far and further substantiated by the following surface science data (Section 3.2). The essential implication, however, is that an ideal dose exists, where both, carbon and oxygen are at lowest levels. Please note that the logarithmic abscissa in Figure 4 leads

to the impression that the ideal dose is very narrow. In numbers, however, the ideal dose ranges between 10 and 20 C/cm^2, which is a factor of 2 and can therefore be easily controlled.

3.2. Surface study under UHV conditions

The results discussed in Section 3.1 show that electron irradiation in presence of H_2O can efficiently remove carbon from FEBID deposits fabricated from $(EtCp)_2Ru$. Surface analysis tools applied under UHV conditions provide insight in the chemistry that underlies the deposit formation and water-assisted purification.[39] In the UHV experiments, thin condensed layers of $(EtCp)_2Ru$ on a Ta substrate held at cryogenic temperature serve as model system. Mass spectrometry (MS) was used to monitor volatile species that evolved during electron irradiation and subsequent temperature increase of the substrate. This allows us to identify contributions of electron-induced and thermal reactions to deposit formation and water-assisted processing.[39] Changes in deposit composition as a result of electron irradiation in presence of H_2O were analyzed by AES.

3.2.1. Electron-induced degradation of multilayer condensed films of $(EtCp)_2Ru$

Model FEBID deposits were prepared from thin layers of $(EtCp)_2Ru$ (13-20 ML) that were condensed on a Ta substrate held at 110 K. The layers were irradiated at 31 eV until ESD of volatile irradiation products ceased, which served as indication that the electron-induced conversion of $(EtCp)_2Ru$ was completed. Volatile products retained on the substrate were then desorbed by increasing the temperature in a TDS experiment to leave behind a non-volatile deposit. The electron energy of 31 eV was selected because (i) it falls in the extended energy range that is typical for secondary electrons (SEs) released when a high energy electron beam impacts on a material and (ii) it is high enough to ascertain a reasonable proceeding speed.

The MS recorded during electron exposure of the condensed $(EtCp)_2Ru$ layer (Figure 5(a)) differs from both, MS of the residual gas recorded prior to irradiation (Figure 5(b)) and MS obtained from the precursor vapor (Figure 5(c)) and thus gives evidence of ESD. The two strong peaks at m/z 16 and 15 are assigned to ESD of methane (CH_4) as supported by their characteristic intensity ratio of 1:0.9.[12,39,47] We rule out contributions of $CH_3^{\bullet}$ because, in contrast to ESD from acetone and acetylacetone,[12] the intensity of m/z 15 does not exceed that of m/z 16. The signal group m/z 26-30 reveals the desorption

of C2 products. Based on reference MS recorded using the same QMS and on literature MS[47] and taking into account absolute ionization cross sections,[48] this pattern is indicative of ESD of ethane (C_2H_6) and ethene (C_2H_4) with relative abundance of 1:4 (see Supporting Information, Figure S13 and Figure S14). Excess intensity of m/z 28 is ascribed to ESD of CO adsorbed as an impurity species from the residual gas. Finally, we also observed a minor ESD signal at m/z 39 ($C_3H_3^+$) and 41 ($C_3H_5^+$) during the initial stages of irradiation, indicative of desorption of a species relating to the Cp ring.[39]

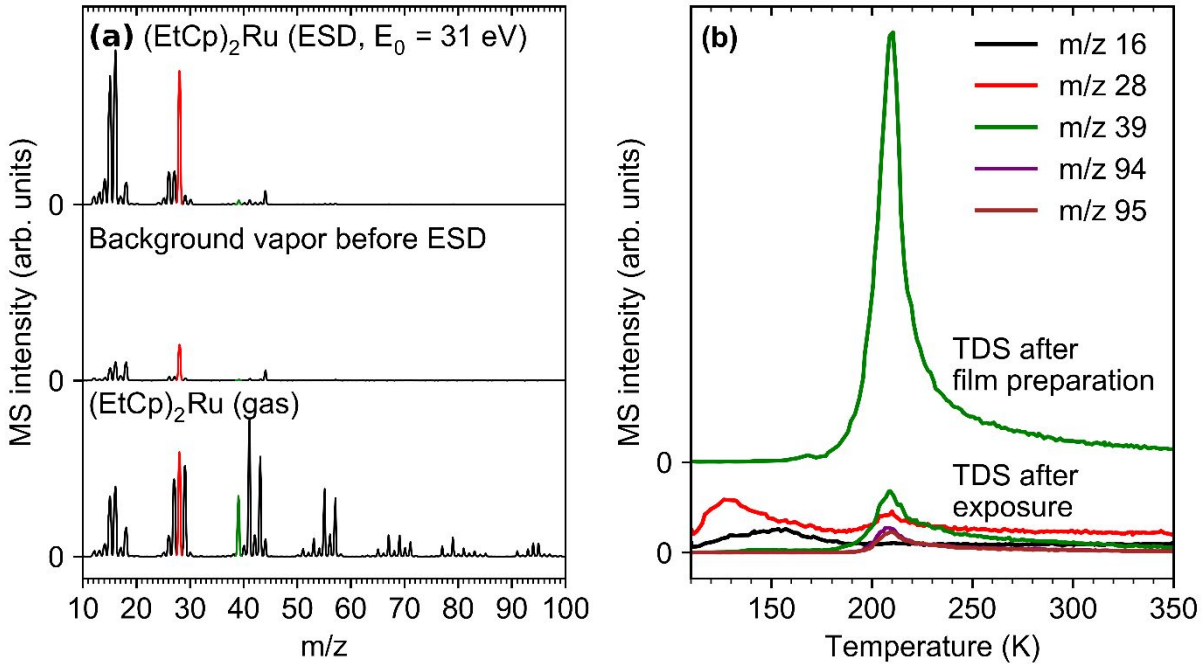

Figure 5. Mass spectra recorded (a) during electron exposure of 40 mC/cm² at $E_0 = 31$ eV of an adsorbed layer of $(EtCp)_2Ru$ with thickness of 13-20 ML on a Ta substrate held at 110 K, (b) before the start of irradiation, and (c) during dosing of $(EtCp)_2Ru$ onto the Ta substrate. (d) TDS experiments performed directly after preparation of the precursor layer and after electron exposure of 40 mC/cm² at $E_0 = 31$ eV. After the temperature ramp terminated at 350 K, the temperature was rapidly increased to 450 K where it was held for 30 s in a final annealing step.

Gas phase data on the electron-induced fragmentation of $(EtCp)_2Ru$ rationalize the observed ESD pattern. At electron energies above the typical molecular ionization threshold of 10 eV, dissociative ionization (DI), as seen in the gas phase electron impact mass spectrum (EI-MS) of $(EtCp)_2Ru$ (Supporting Information, Figure S15), initiates the formation of products. The most intense signal in the EI-MS at m/z 273 ($[M\text{-}CH_3]^+$) stems from β-cleavage on the ethyl group. In the adsorbed layer, the

released $CH_3^{\bullet}$ radicals can intra- or intermolecularly abstract H from $(EtCp)_2Ru$ molecules thus explaining ESD of CH_4. In line with ESD, EI-MS also shows the loss of C_2H_6 ($[M-30]^{\bullet+}$ at m/z 258) or C_2H_4 ($[M-28]^{\bullet+}$ at m/z 260) due to α-cleavage of the ethyl group from the ring, in line with previous data on ferrocenes[49] and hydrogen transfer from or to the ethyl group. The fact that C_2H_4 is dominant over C_2H_6 in ESD from $(EtCp)_2Ru$ (Supporting Information, Figure S13 and Figure S14) while the opposite is seen in EI-MS (Supporting Information, Figure S15) suggests that intermolecular H transfer contributes to ESD. This includes H transfer between $CH_3^{\bullet}$ and $C_2H_5^{\bullet}$ radicals leading to CH_4 and C_2H_4 or between two $C_2H_5^{\bullet}$ radicals yielding C_2H_4 and C_2H_6. EI-MS (Supporting Information, Figure S15) also shows two complementary signals at m/z 95 ($C_7H_{11}^+$) and 193 ($C_7H_7Ru^+$), indicating that the charge may reside on either of the fragments. This type of fragmentation rationalizes the desorption of a species relating to the Cp ring as implied by the weak ESD signals at m/z 39 ($C_3H_3^+$) and 41 ($C_3H_5^+$). To support this interpretation, we note that the absence of a signal relating to the Cp ring in ESD from $MeCpPtMe_3$[39,50] correlates with a particularly low intensity of signals related to the loss of the Cp ring from this compound in EI-MS.[51] However, m/z 95 ($C_7H_{11}^+$) and 193 ($C_7H_7Ru^+$) species, when released in the condensed phase, can potentially attack adjacent molecules to induce crosslinking of the ligands. This explains the relatively weak intensity of the Cp ring fragments at m/z 39 and 41 in ESD from $(EtCp)_2Ru$.

Dissociative electron attachment (DEA) is prominent at electron energies below the ionization threshold.[5,7] Under the present conditions, SEs released by the ionization processes described above may initiate DEA. However, DEA is not a likely explanation for the ESD signals relating to the Cp ring because, as known from different late transition metal cyclopentadienyl complexes, the cross section for the loss of a Cp ligand after electron attachment is small.[52] Equally, the Cp ring preferentially remains on the metal in DEA to precursors containing different types of ligands.[51,53,54]

The dominance of CH_4, C_2H_4, and C_2H_6 in ESD with only weak signals of the Cp ring rationalizes the large amounts of carbon incorporated in deposits produced from $(EtCp)_2Ru$ in FEBID (Section 3.1). In fact, the previously reported deposit composition RuC_9[25] corresponds to most of the carbon of the Cp rings after loss of the side groups. A post-exposure TDS experiment was performed to check if thermal

reactions further enhance the deposit purity in FEBID. The electron irradiation of the $(EtCp)_2Ru$ layer was thus stopped after an exposure of 40 mC/cm² where the ESD intensities at characteristic m/z ratios had returned to the baseline level (Supporting Information, Figure S16). The subsequent TDS shows that the m/z 39 desorption signal of the precursor at 210 K has been strongly reduced (Figure 5(d)). The remaining intensity is ascribed to either a small amount of unreacted $(EtCp)_2Ru$ or to a structurally related compound resulting from fragmentation of the side groups. The loss of volatile species during ESD has thus in fact converted the $(EtCp)_2Ru$ layer into a less volatile state. We note that the m/z 39 TDS curve does not reveal signals at lower temperature that would point to desorption of a Cp-related species but the m/z 28 curve shows a broad desorption signal in the range 110-140 K (Figure 5(d)). m/z 28 is attributed to the volatile C2 species retained in the deposit at cryogenic temperature after irradiation. However, further thermal evolution of volatile products above the desorption temperature of $(EtCp)_2Ru$ was not observed during TDS. Therefore, and in contrast to the case of $MeCpPtMe_3$ where CH_4 was thermally released in a temperature range extending beyond room temperature,[39] the model deposits formed by combined ESD and TDS from $(EtCp)_2Ru$ should closely resemble the material produced in the actual room temperature FEBID process. This also emphasizes the need for purification processes in the case of $(EtCp)_2Ru$.

3.2.2. Volatile products released during water-assisted purification of a model $(EtCp)_2Ru$ deposit

The deposits prepared from $(EtCp)_2Ru$ by electron irradiation (ESD), warming up (TDS), and annealing at 450 K for 30 s (see Section 3.2.1) were subject to repeated cycles of water-assisted purification. In each of these cycles, H_2O was condensed on the deposit held at 110 K followed by exposure to 31 eV electrons at the same temperature. During this IDS and ESD sequence, the gas phase was monitored by repeated rapid mass scans. After irradiation, the deposit temperature was increased to 450 K during a TDS run and finally held at 450 K for 30 s. The deposit composition was determined by AES performed at room temperature after selected purification cycles.

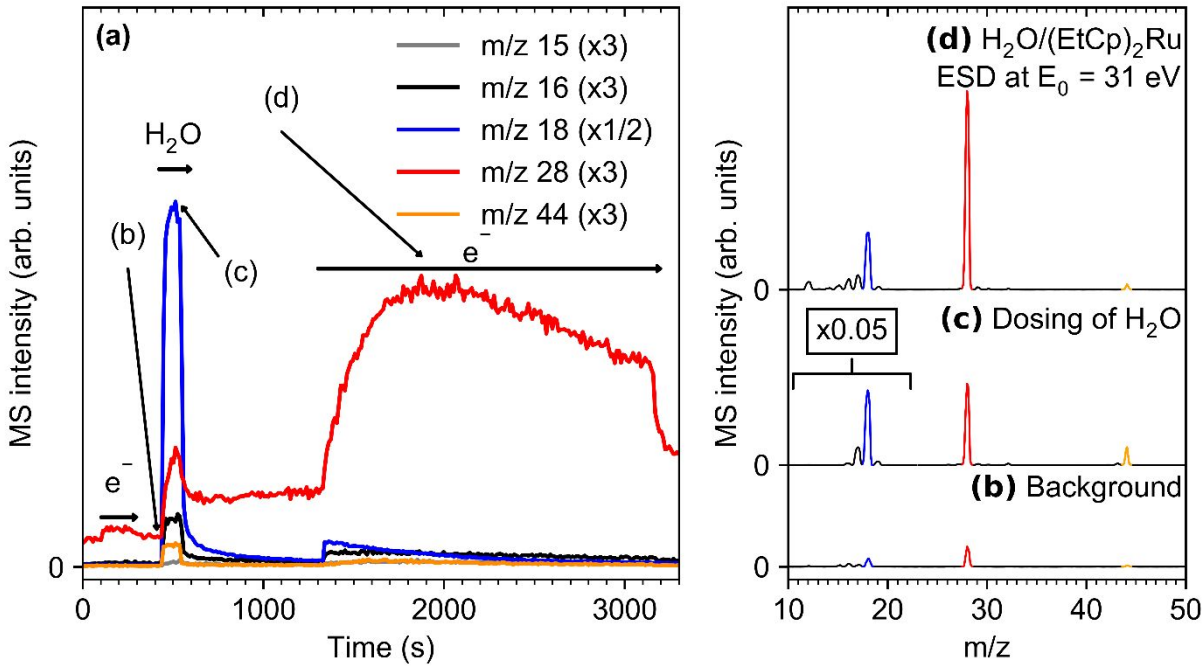

Figure 6. (a) Isothermal and electron-stimulated desorption spectrum (ISD and ESD) extracted from a sequence of rapid mass scans recorded during a water-assisted purification model experiment on a $(EtCp)_2Ru$ deposit. The deposit was produced beforehand by irradiating a 13-20 ML film of $(EtCp)_2Ru$ at E_0 = 31 eV until the production of volatile products in ESD had ceased (40 mC/cm²). The deposit was annealed to 450 K for 30 s and cooled back to 110 K before acquiring the data shown. A short electron exposure (100-300 s, 31 eV, 2 mC/cm², marked by e^-) was applied at the beginning of the purification experiment to verify that no further ESD occurred. A total amount of 40-80 ML H_2O was then dosed onto the deposit held at 110 K (400-600 s, marked by H_2O). Finally, a further electron exposure (1300-3150 s, 31 eV, 20 mC/cm², marked by e^-) was performed at the same temperature. Representative mass scans show the gas phase composition (b) immediately before dosing H_2O, (c) during H_2O dosing, and (d) at the maximum of CO evolution (m/z 28) during the final electron exposure step. The m/z 10-20 range in (b) is scaled to 0.05% of its actual intensity to enhance the visibility of less intense signals.

Figure 6 illustrates a purification cycle performed on a freshly prepared deposit by tracing the temporal evolution of characteristic m/z ratios (Figure 6(a)). Also shown are representative MS obtained immediately before (Figure 6(b)) and during H_2O dosing (Figure 6(c)) as well as during the subsequent electron exposure step (Figure 6(d)). Before dosing H_2O, a short irradiation was carried out (Figure 6(a), 100-300 s) to verify that ESD had in fact ceased. Apart from a very small amount of residual CO, the absence of any onset in the mass traces m/z 15, 16, 18, and 44 and the very low intensities of these signals in the MS (Figure 6(b)) give evidence that no volatile irradiation products were emitted from the

deposit film *via* ESD beyond the initial irradiation of the intact precursor layer and the subsequent annealing step. Dosing of H_2O on the $(EtCp)_2Ru$ deposit then led to desorption of CO and some CO_2 (Figure 6(a), 400-600 s). These stem indeed from the deposit as supported by a control experiment in which H_2O was dosed onto the freshly sputtered and subsequently irradiated Ta substrate. The control showed much smaller signals (Supporting Information, Figure S17), ruling out that CO and CO_2 are formed predominantly on hot filaments or are co-dosed from the gas-handling manifold. Signals at m/z 26, 27, 29 and 30 were absent (Figure 6(c)) giving evidence that formation of C2 hydrocarbons was negligible during this step. The prominent m/z 18 ($H_2O^{\bullet+}$) signal and a small signal at m/z 16 ($O^{\bullet+}$) show the same temporal behavior during H_2O dosing (see Figure 6(a)) indicating that both relate to H_2O. In line with this, a significant increase of the m/z 15 signal was not observed (Figure 6(a) and (c)) so that formation of CH_4 can be ruled out.

The CO desorption signal increased steadily during dosing of H_2O and decayed when the supply of H_2O was stopped (Figure 6(a)). CO thus forms through a thermal reaction of H_2O with the $(EtCp)_2Ru$ deposit even in absence of electron irradiation. However, the subsequent electron irradiation step led not only to desorption of H_2O (m/z 18) but also to much more prominent release of CO (m/z 28) than the thermal reaction alone (Figure 6(a), 1300-3150 s) with other volatile products being again negligible (Figure 6(d)). Hence, CO is the main volatile product formed during water-assisted electron beam purification of deposits produced from $(EtCp)_2Ru$. The loss of material observed as decrease of the deposit thickness in Section 3.1 thus proceeds *via* conversion to CO. We note that – despite the fact that the mass curve for m/z 18 leveled off after 20 mC/cm² (Figure 6(a)) – H_2O was still present in the deposit as indicated by a respective desorption signal at ~155 K in a post-purification TDS (Supporting Information, Figure S18).

The production of CO *via* thermal reactions at 110 K points to the existence of reactive sites in the deposit. Note that hydrolysis of intact $MeCpPtMe_3$ was not observed under the same experimental conditions.[39] Reactions of H_2O with intact $(EtCp)_2Ru$ can thus be ruled out because the Ru center is even more sterically shielded by the two EtCp ligands. It is conceivable that the loss of CH_4 and C2 hydrocarbons during electron exposure of $(EtCp)_2Ru$ (see Section 3.2.1.) leaves behind radical sites on

the Cp rings that can abstract hydrogen from H_2O. This, in turn produces reactive $^{\bullet}OH$ radicals[55] that further oxidize the hydrocarbon residue in the deposit to eventually form CO. However, small amounts of Cp-containing products already desorbed as well during deposit formation (Figure 5(a)). This would leave behind Ru sites that are accessible to H_2O and may expose the known catalytic activity of this metal.[56-58] We note that Ru-containing catalysts enhance the water-gas shift reaction that transforms CO and H_2O to CO_2 and H_2[57,58] which might also contribute to the formation of small amounts of CO_2 as seen in Figure 6(c). The catalytic activity of Ru may thus be relevant to the water-assisted purification of Ru deposits as studied here. We also observe that desorption leveled off when dosing of H_2O was terminated except for CO (Figure 6(a)). In fact, the m/z 28 trace decayed only partially to stabilize at a level significantly above the pre-dosing value with even a small intensity increase over time (700-1200 s). This points towards slow diffusion of H_2O into the deposit and consequent reaction with reactive sites located at a larger depth. We note that CO desorption did not decay after dosing of H_2O in an experiment performed on a deposit produced without subsequent annealing (Supporting Information, Figure S19). We attribute this to a larger number of reactive sites in the deposit. Thermal activation as provided by annealing prior to dosing of H_2O (Figure 6) increases the mobility of species in the deposit so that radical sites produced beforehand by electron exposure can recombine. In consequence, the present results imply that temperature increase may not have a favorable effect on the water-assisted purification of FEBID deposits produced from $(EtCp)_2Ru$.

Turning to the electron-induced CO production after dosing of H_2O, we note that ESD of H_2O increased sharply at the start of irradiation to level off immediately. In contrast, desorption of CO increased during approximately 400 s before starting to decline very slowly (Figure 6(a), 1300-3150 s). As described previously,[39] this behavior indicates that CO formation proceeds *via* an intermediate product that is formed in an electron-induced reaction of the deposit with H_2O. As a first step, electron exposure of condensed H_2O at E_0 above the ionization threshold leads to intermolecular proton transfer according to (1).[59]

$$H_2O^{\bullet+} + H_2O \rightarrow H_3O^+ + {}^{\bullet}OH \qquad (1)$$

Anionic ligands such as $EtCp^-$ can be cleaved off from the central metal when metallocenes are protonated.[60] Following ionization, $H_2O^{\bullet+}$ can thus initiate reaction (2), where the intact precursor also represents Cp-containing irradiation products retained in the deposit.

$$H_2O^{\bullet+} + (EtCp)_2Ru \rightarrow EtCpH + EtCpRu^+ + {}^{\bullet}OH \quad (2)$$

The reaction products of (2) can again lead to removal of carbon from $(EtCp)_2Ru$ deposits. Protonation and loss of EtCpH yields a cationic $EtCpRu^+$ species with the Ru center again accessible to further reactions. Cationic Ru complexes are known to be highly efficient in oxidation reactions of various species, i.a. hydrocarbons.[61] Also, $^{\bullet}OH$ radicals again act as oxidizing species in the deposit. Furthermore, $H_2O^{\bullet+}$ can add to one of the C=C double bonds of EtCpH yielding an alcohol.[39,55] As known for methanol, alcohols can release CO upon electron irradiation.[62] This reaction sequence explains the delayed desorption of CO during electron exposure of the deposits. We thus propose that, in analogy to the previous study on $MeCpPtMe_3$,[39] electron irradiation leads to addition of H_2O to a C=C double bond in a Cp moiety and subsequent loss of CO from this intermediate. This contributes to the removal of carbon from the deposit. This is a relevant scenario because it explains uptake of oxygen during phase 1 of the purification process accompanied by the initial swelling of the deposit, both of which cannot be explained by mere uptake of H_2O (see Section 3.1).

The progress of deposit purification with increasing number of purification cycles was deduced from the amount of CO that desorbed in ESD and, after selected cycles, from the deposit composition *via* AES (Figure 7(a) and (b)). For this purpose, a deposit was prepared in the same way as described above and exposed to 24 cycles of water-assisted purification cycles as shown in Figure 6(a) but without repeated electron irradiation prior to dosing of H_2O. The amount of CO that evolved in each cycle during the 20 mC/cm^2 electron exposure after H_2O dosing was quantified by integrating the m/z 28 signal intensities over purification time (Figure 7(b)).

AES shows signals of the underlying Ta substrate, of the precursor, and of oxygen introduced as H_2O during the purification cycles. The Ta NNN signals at kinetic energies of 175 eV and 183 eV[41] (marked in green in Figure 7(a)) were the only signals after sputter-cleaning of the substrate pointing to a clean surface prior to deposit formation. After dosing of $(EtCp)_2Ru$, electron irradiation and post-exposure

TDS, a broad signal of the precursor at ~275 eV was observed instead (marked in yellow in Figure 7(a)). Due to limited spectral resolution, the Ru MNN (277 eV) and C KLL (275 eV) AES signals[41] cannot be separated. With ongoing purification (top five spectra in Figure 7(a) representative of exposures in the range 20-480 mC/cm²), the total intensity of this combined Ru/C signal decreased by 44% in total, indicative of an average intensity loss of 2% per cycle of 20 mC/cm². Based on the tabulated sensitivity factors of the Ru MNN (277 eV) and C KLL (275 eV) signals[41] and assuming a homogeneous distribution of Ru and C with a composition of RuC_9[25] in the deposit, 30% of the intensity of the Ru/C signal prior to purification can be ascribed to Ru and 70% to C. We deduce that roughly 60% of the initial carbon content has been removed after an electron exposure of 480 mC/cm² in presence of H_2O. This estimate changes by less than 5% when it is based on the initial precursor composition of RuC_{14}.

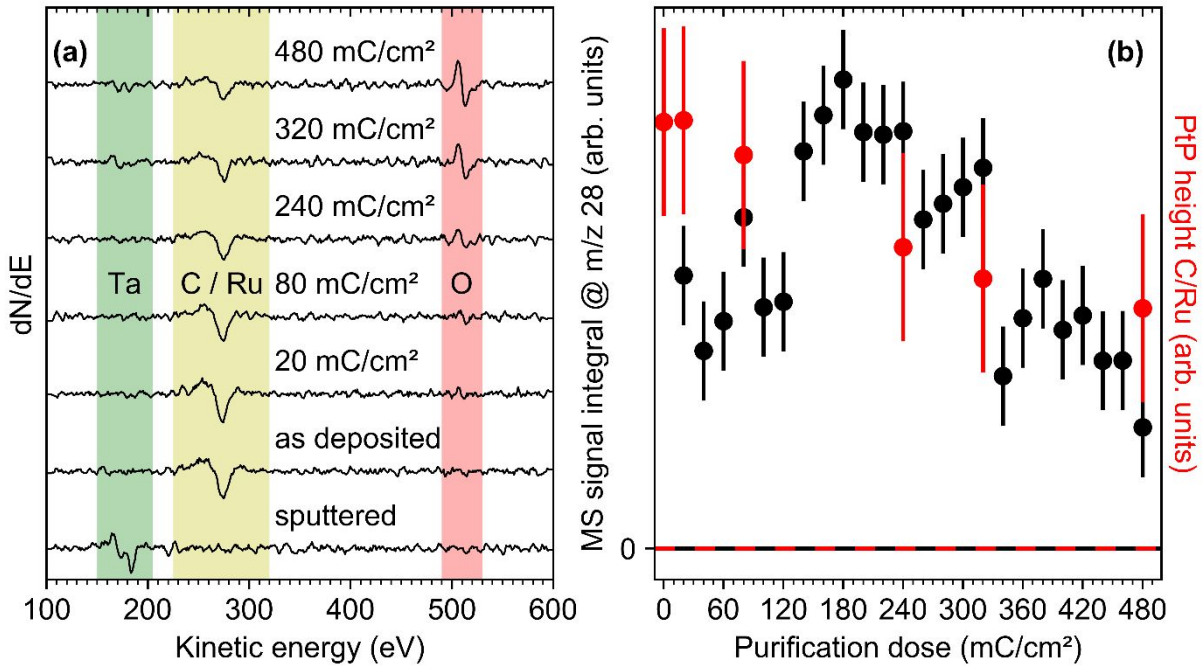

Figure 7. (a) Derivative AES of the freshly sputtered Ta sheet, an as-deposited $(EtCp)_2Ru$ layer (after 40 mC/cm² at E_0 = 31 eV), and the same layer after selected purification exposures of up to 480 mC/cm² in total. Overall, 24 purification cycles were carried out, each involving electron exposure of 20 mC/cm² at E_0 = 31 eV in the presence of 20-40 ML or 40-80 ML H_2O condensed on the deposit and followed by annealing to 450 K. (b) Plot of the total Peak-to-Peak (PtP) height of the C/Ru AES signal (red) and the total IDS CO signal (as integrated desorption signal on m/z 28, black) against purification exposure. Note that the third and the sixth purification cycle applied only 20-40 ML H_2O to the deposit whereas the remaining cycles were carried out with 40-80 ML H_2O.

In line with the clean UHV environment, the O KLL signal was below the detection limit in the as-prepared deposit indicating that oxygen-free deposition from $(EtCp)_2Ru$ is feasible in a clean environment. However, starting at a purification exposure of ~80 mC/cm², the O KLL signal (510 eV) began to increase (marked in red in Figure 7(a)),[41] pointing to incorporation of oxygen in the deposit proposed above and also in Section 3.1 to stem from oxygenated species in the deposit. Generally, the Ta substrate is also prone to oxidation. However, the deposit was initially thick enough to effectively screen signals from the underlying substrate. Only at higher purification exposures (320 mC/cm² and above), the Ta NNN signals reappeared with low intensity, indicating a decreasing deposit thickness in line with the observed removal of carbon. In this regime oxidation of the Ta substrate very likely contributes to the increase of the O KLL signal.

Monitoring the removal of carbon through the evolution of CO during electron exposure of the purification cycles (Figure 7(b)) revealed that the amount of desorbing CO increased during the first cycles to peak at intermediate purification exposures around 180 mC/cm², i.e. when already roughly 30% of the initial carbon content was removed according to AES. For high purification exposures, the amount of CO per cycle again decreased in line with the decreasing amount of carbon as indicated by AES. The initial increase of CO production for low exposures is also in line with the proposed formation of oxygenated intermediates that are the actual source from which CO is finally released. We further propose that in the UHV experiment, the electron exposure during a specific purification cycle is insufficient to degrade the entire amount of oxygenated intermediates and these do not desorb during TDS and annealing when formed on already crosslinked ligands. The oxygenated intermediates thus accumulate during several cycles before, due to depletion of the initial carbon material, their production rate drops below the rate of their decomposition to CO. We thus ascribe not only the delayed ESD of CO during a single purification cycle (Figure 6(a)) but also the increase of the CO production rate during the early purification cycles (Figure 7(b)) to the slow build-up of oxygen-containing intermediates before the carbon residue is depleted due to loss of CO. Both are reminiscent of the initial phase 1 of deposit purification following FEBID before the actual removal of the carbon matrix sets in (see Section 3.1).

3.3. Comparison between deposit purification in the DBM and in UHV

Despite the fundamentally different experimental conditions (see also Supporting Information, Table S1), we have shown in Sections 3.1 and 3.2 that the deposit purification as observed in the DBM in LP mode and in the UHV setup can be correlated in terms of the underlying electron-induced chemistry. However, a quantitative comparison is not easy. In contrast to the UHV study, it is not possible to estimate the actual amount of H_2O in contact with the deposit in the DBM experiment because the sticking coefficient on the deposit at room temperature is unknown. Also, a direct comparison of the electron current densities is not meaningful because the cross section for fragmentation of the precursor depends on the electron energy and secondary electrons (SEs) make a large contribution in the DBM process. Nonetheless, the removal of carbon proceeds at a similar rate with respect to electron exposure in both experiments. After applying 0.48 C cm^{-2} in the UHV experiment, the carbon content was reduced by roughly 60% (Figure 7(b) and discussion in Section 3.2). In the DBM and for a deposit thickness that was approximately ten times larger than in the UHV experiment (see Table S1), near 8 C cm^{-2} were required to achieve a similar reduction of the carbon content (see Figure 4). This reveals that not only the chemistry but also the efficiency of carbon removal is similar in the two experiments despite the large differences in the experimental conditions.

A possible explanation for the similar purification efficiency in both experiments is that SEs with energies similar to those used in the UHV experiment also initiate most of the chemistry in the FEBID process performed with 5 keV electrons. However, an excess of H_2O in the purification process is also important. As shown previously in the case of $MeCpPtMe_3$, variation of the partial H_2O pressure during electron beam purification did not change the rate at which carbon was removed indicative of an electron-limited process.[22,23] This is not reflected by the ratio of electron and H_2O flux (Supporting Information, Table S1), the former being larger by an order of magnitude, underlining that such figures are meaningless without knowledge of the sticking coefficient of H_2O and the electron energy dependent cross sections for the relevant electron-induced reactions. Also, even if electrons impinge in large excess, precursor fragmentation is only initiated by a fraction of those and many electrons are simply scattered into or from the material. In the UHV experiment, H_2O was clearly not depleted in the

individual purification cycles as obvious from TDS performed after the ESD step (Supporting Information, Figure S18), again pointing to an electron-limited process. Here, this limitation also derives from the limited penetration depth of low-energy electrons. In fact, the mean free path (MFP) of 31 eV electrons as used in the UHV experiments amounts to only a few Å.[63] H_2O observed in TDS after ESD had ceased most likely stems from deeper layers of the deposit pointing to diffusion into the deposit. The facile diffusion of H_2O into a carbonaceous deposit, which is contrary to the behavior of O_2 when used as purification reagent,[64] was also demonstrated in simulations[65] and in experiments on the water-assisted purification of deposits produced from $MeCpPtMe_3$.[65] As a result of this mobility, the deposit in the UHV experiment acts as reservoir that supplies H_2O and thus enables formation of CO while electron irradiation proceeds (Figure 6).

These common aspects of the DBM and UHV experiments, namely, the role of low energy electrons and the diffusion of an excess of H_2O into the deposit, enable the chemical reactions involved in the water-assisted purification process as discussed in the previous sections. This further rationalizes our conclusion that the same reactions as monitored in UHV are in fact also relevant in the actual FEBID purification process and thus supports the relevance of surface science model experiments for an in-depth understanding of deposit purification processes.

4. Conclusion

The results obtained herein provide evidence that carbon-rich FEBID deposits produced from $(EtCp)_2Ru$ can be successfully converted to a dense Ru nanomaterial by electron exposure in the presence of H_2O vapor. During the purification process, the deposit shrinks in the vertical dimension by about 90% while both, footprints and qualitative 3D surface shapes are preserved. While the evolution of the inner structure is very similar to Pt- and Au-based FEBID materials (bottom up grain-growth / coalescence and densification without any evidence of pores and cracks),[22,23] an ideal dose range exists for Ru before oxidation becomes dominant due to a strong excess of electrons together with dissociated H_2O. This is a clear advantage as compared to an O_2-based purification process during which the oxygen content increased continuously.[25] Although an exact determination of remaining oxygen and carbon levels is

pending due to technical challenges on that scale, the collective insight *via* SEM, AFM, EDX and TEM suggests very low remaining impurity levels. The relevant stages of the deposit purification, namely, an initial period during which the deposit swells followed by a rapid removal of carbon correlate well with the results from UHV surface science studies.

The UHV model experiments, performed on multilayer condensed layers of $(EtCp)_2Ru$, complement the FEBID and subsequent water-assisted processing by providing insight into the chemical reactions that underlie deposit formation and purification. According to ESD results, the electron-induced fragmentation of the precursor leads predominantly cleaves the side chains from the ligands. This rationalizes the previously reported composition RuC_9 of FEBID deposits fabricated from $(EtCp)_2Ru$.[25] Electron irradiation of the deposit in presence of H_2O leads to exclusive desorption of CO together with minor amounts of CO_2. However, thermal reactions do not play a significant role in the purification process which implies that an elevated temperature is unlikely to improve the purity of the thus obtained deposits. In line with a mechanism formulated earlier for $MeCpPtMe_3$,[39] we propose that the formation of CO involves oxygenated intermediates deriving from an electron-induced reaction of H_2O with the carbon residue in the deposit. In the DBM experiment, this result is reflected in a temporary increase of the oxygen content as well as a swelling of the deposit during the early stages of the purification process before removal of carbon sets in.

Despite the very different conditions in terms of temperature, electron energy, electron current density, water dosing process, and deposit thickness, the present results reveal the correlation between the purification processes in the DBM and in UHV, which can be understood based on the underlying electron-induced chemistry. Also, the electron exposures required to achieve a similar level of purification are surprisingly similar in the UHV model experiment and in the actual deposit purification in the DBM. This supports that low energy electrons as released under the impact of a high-energy electron beam and the rapid diffusion of H_2O into the deposit are essential factors in the purification process.

Overall, we conclude that water assisted electron beam purification of $(EtCp)_2Ru$ based FEBID materials is a promising candidate on the route towards pure Ru nanomaterials for on-demand applications such

as EUVL mask repair or modification. The combined efforts in this study enabled a fundamental understanding of the underlying chemical processes, which, in turn, acts as baseline for further improvements.

Associated Content

Supporting Information

The Supporting Information is available free of charge on the ACS Publications website at DOI: 10.1021/acs.XXX.

Further ESD, IDS, TDS, EI-MS, SEM, AFM, EDX data as well as results from CASINO simulations (PDF).

Acknowledgements

MR and PS gratefully acknowledge financial support from the DFG (Project Number Sw26/13-2). This work was conducted within the framework of the COST Action CM1301 (CELINA). The authors are grateful to the mass spectrometry lab of the department 2 of the University of Bremen for recording sector mass scans of $(EtCp)_2Ru$. RW, DK and HP gratefully acknowledge the valuable support provided from Ferdinand Hofer, Sebastian Rauch and Cornelia Trummer. The financial support by the Austrian Federal Ministry for Digital and Economic Affairs and the National Foundation for Research, Technology and Development is gratefully acknowledged.

Author Information

*E-mail: m.rohdenburg@uni-bremen.de. Phone: +49 421 218 63203 (M.R.).

*E-mail: swiderek@uni-bremen.de. Phone: +49 421 218 63200 (P.S.).

Notes

The authors declare no competing financial interest.

References

(1) Utke, I.; Hoffmann, P.; Melngailis, J. Gas-Assisted Focused Electron Beam and Ion Beam Processing and Fabrication. *J. Vac. Sci. Technol. B Microelectron. Nanom. Struct.* **2008**, *26* (4), 1197.

(2) Huth, M.; Porrati, F.; Schwalb, C.; Winhold, M.; Sachser, R.; Dukic, M.; Adams, J.; Fantner, G. Focused Electron Beam Induced Deposition: A Perspective. *Beilstein J. Nanotechnol.* **2012**, *3* (1), 597–619.

(3) Swiderek, P.; Marbach, H.; Hagen, C. W. Chemistry for Electron-Induced Nanofabrication. *Beilstein J. Nanotechnol.* **2018**, *9*, 1317–1320.

(4) *Nanofabrication Using Focused Ion and Electron Beams: Principles and Applications*, Russell, P.; Utke, I.; Moshkalev, S., Eds.; Oxford University Press: New York, **2012**.

(5) Fairbrother D.H., Rosenberg S.G., Hagen C.W., Utke I., Swiderek P. Focused Electron Beam-Induced Processing. In *Low-Energy Electrons: Fundamentals and Applications*; Ingólfsson, O., Ed.; Jenny Stanford Publishing: Singapore, **2019**.

(6) Spencer, J. A.; Rosenberg, S. G.; Barclay, M.; Wu, Y.-C.; McElwee-White, L.; Howard Fairbrother, D. Understanding the Electron-Stimulated Surface Reactions of Organometallic Complexes to Enable Design of Precursors for Electron Beam-Induced Deposition. *Appl. Phys. A* **2014**, *117* (4), 1631–1644.

(7) Thorman, R. M.; Kumar T. P., R.; Fairbrother, D. H.; Ingólfsson, O. The Role of Low-Energy Electrons in Focused Electron Beam Induced Deposition: Four Case Studies of Representative Precursors. *Beilstein J. Nanotechnol.* **2015**, *6* (1), 1904–1926.

(8) Hampden-Smith, M. J.; Kodas, T. T. Chemical Vapor Deposition of Metals: Part 1. An Overview of CVD Processes. *Chem. Vap. Depos.* **1995**, *1* (1), 8–23.

(9) George, S. M. Atomic Layer Deposition: An Overview. *Chem. Rev.* **2010**, *110* (1), 111–131.

(10) Johnson, R. W.; Hultqvist, A.; Bent, S. F. A Brief Review of Atomic Layer Deposition: From Fundamentals to Applications. *Mater. Today* **2014**, *17* (5), 236–246.

(11) Botman, A.; Mulders, J. J. L.; Hagen, C. W. Creating Pure Nanostructures from Electron-Beam-Induced Deposition Using Purification Techniques: A Technology Perspective. *Nanotechnology* **2009**, *20* (37), 372001.

(12) Warneke, J.; Van Dorp, W. F.; Rudolf, P.; Stano, M.; Papp, P.; Matejčík, Š.; Borrmann, T.; Swiderek, P. Acetone and the Precursor Ligand Acetylacetone: Distinctly Different Electron Beam Induced Decomposition? *Phys. Chem. Chem. Phys.* **2015**, *17* (2), 1204–1216.

(13) Warneke, J.; Rohdenburg, M.; Zhang, Y.; Orszagh, J.; Vaz, A.; Utke, I.; De Hosson, J. T. M.; van Dorp, W. F.; Swiderek, P. Role of NH_3 in the Electron-Induced Reactions of Adsorbed and Solid Cisplatin. *J. Phys. Chem. C* **2016**, *120* (7), 4112–4120.

(14) Rohdenburg, M.; Martinović, P.; Ahlenhoff, K.; Koch, S.; Emmrich, D.; Gölzhäuser, A.; Swiderek, P. Cisplatin as a Potential Platinum Focused Electron Beam Induced Deposition Precursor: NH_3 Ligands Enhance the Electron-Induced Removal of Chlorine. *J. Phys. Chem. C* **2019**, *123* (35), 21774–21787.

(15) Kolb, F.; Schmoltner, K.; Huth, M.; Hohenau, A.; Krenn, J.; Klug, A.; List, E. J. W.; Plank, H. Variable Tunneling Barriers in FEBID Based PtC Metal-Matrix Nanocomposites as a Transducing Element for Humidity Sensing. *Nanotechnology* **2013**, *24* (30), 305501.

(16) Dukic, M.; Winhold, M.; Schwalb, C. H.; Adams, J. D.; Stavrov, V.; Huth, M.; Fantner, G. E. Direct-Write Nanoscale Printing of Nanogranular Tunnelling Strain Sensors for Sub-Micrometre Cantilevers. *Nat. Commun.* **2016**, *7* (1), 12487.

(17) Spencer, J. A.; Wu, Y.-C.; McElwee-White, L.; Fairbrother, D. H. Electron Induced Surface Reactions of Cis-$Pt(CO)_2Cl_2$: A Route to Focused Electron Beam Induced Deposition of Pure Pt Nanostructures. *J. Am. Chem. Soc.* **2016**, *138* (29), 9172–9182.

(18) Landheer, K.; Rosenberg, S. G.; Bernau, L.; Swiderek, P.; Utke, I.; Hagen, C. W.; Fairbrother, D. H. Low-Energy Electron-Induced Decomposition and Reactions of Adsorbed Tetrakis(Trifluorophosphine)Platinum [$Pt(PF_3)_4$]. *J. Phys. Chem. C* **2011**, *115* (35), 17452–17463.

(19) Botman, A.; Mulders, J. J. L.; Weemaes, R.; Mentink, S. Purification of Platinum and Gold Structures after Electron-Beam-Induced Deposition. *Nanotechnology* **2006**, *17* (15), 3779–3785.

(20) Mehendale, S.; Mulders, J. J. L.; Trompenaars, P. H. F. A New Sequential EBID Process for the Creation of Pure Pt Structures from $MeCpPtMe_3$. *Nanotechnology* **2013**, *24* (14), 145303.

(21) Plank, H.; Noh, J. H.; Fowlkes, J. D.; Lester, K.; Lewis, B. B.; Rack, P. D. Electron-Beam-Assisted Oxygen Purification at Low Temperatures for Electron-Beam-Induced Pt Deposits: Towards Pure and High-Fidelity Nanostructures. *ACS Appl. Mater. Interfaces* **2014**, *6* (2), 1018–1024.

(22) Geier, B.; Gspan, C.; Winkler, R.; Schmied, R.; Fowlkes, J. D.; Fitzek, H.; Rauch, S.; Rattenberger, J.; Rack, P. D.; Plank, H. Rapid and Highly Compact Purification for Focused Electron Beam Induced Deposits: A Low Temperature Approach Using Electron Stimulated H_2O Reactions. *J. Phys. Chem. C* **2014**, *118* (25), 14009–14016.

(23) Winkler, R.; Schmidt, F.-P.; Haselmann, U.; Fowlkes, J. D.; Lewis, B. B.; Kothleitner, G.; Rack, P. D.; Plank, H. Direct-Write 3D Nanoprinting of Plasmonic Structures. *ACS Appl. Mater. Interfaces* **2017**, *9* (9), 8233–8240.

(24) Shawrav, M. M.; Taus, P.; Wanzenboeck, H. D.; Schinnerl, M.; Stöger-Pollach, M.; Schwarz, S.; Steiger-Thirsfeld, A.; Bertagnolli, E. Highly Conductive and Pure Gold Nanostructures Grown by Electron Beam Induced Deposition. *Sci. Rep.* **2016**, *6*, 34003.

(25) Noh, J. H.; Stanford, M. G.; Lewis, B. B.; Fowlkes, J. D.; Plank, H.; Rack, P. D. Nanoscale Electron Beam-Induced Deposition and Purification of Ruthenium for Extreme Ultraviolet Lithography Mask Repair. *Appl. Phys. A* **2014**, *117* (4), 1705–1713.

(26) Rosen, R. S.; Viliardos, M. A.; Kassner, M. E.; Stearns, D. G.; Vernon, S. P. Thermal Stability of Mo/Si Multilayers. In *Proc.SPIE*; 1992; Vol. 1547.

(27) Slaughter, J. M.; Schulze, D. W.; Hills, C. R.; Mirone, A.; Stalio, R.; Watts, R. N.; Tarrio, C.; Lucatorto, T. B.; Krumrey, M.; Mueller, P.; Charles, M. F. Structure and Performance of Si/Mo Multilayer Mirrors for the Extreme Ultraviolet. *J. Appl. Phys.* **1994**, *76* (4), 2144–2156.

(28) Vernon, S. P.; Stearns, D. G.; Rosen, R. S. Chirped Multilayer Coatings for Increased X-Ray Throughput. *Opt. Lett.* **1993**, *18* (9), 672–674.

(29) Barbee, T. W.; Mrowka, S.; Hettrick, M. C. Molybdenum-Silicon Multilayer Mirrors for the Extreme Ultraviolet. *Appl. Opt.* **1985**, *24* (6), 883–886.

(30) Rosen, R. S.; Stearns, D. G.; Viliardos, M. A.; Kassner, M. E.; Vernon, S. P.; Cheng, Y. Silicide Layer Growth Rates in Mo/Si Multilayers. *Appl. Opt.* **1993**, *32* (34), 6975–6980.

(31) Carden, W. G.; Lu, H.; Spencer, J. A.; Fairbrother, D. H.; McElwee-White, L. Mechanism-Based Design of Precursors for Focused Electron Beam-Induced Deposition. *MRS Commun.* **2018**, *8* (2), 343–357.

(32) Spencer, J. A.; Brannaka, J. A.; Barclay, M.; McElwee-White, L.; Fairbrother, D. H. Electron-Induced Surface Reactions of η^3-Allyl Ruthenium Tricarbonyl Bromide [$(\eta^3\text{-}C_3H_5)Ru(CO)_3Br$]: Contrasting the Behavior of Different Ligands. *J. Phys. Chem. C* **2015**, *119* (27), 15349–15359.

(33) Thorman, R. M.; Brannaka, J. A.; McElwee-White, L.; Ingólfsson, O. Low Energy Electron-Induced Decomposition of $(\eta^3\text{-}C_3H_5)Ru(CO)_3Br$, a Potential Focused Electron Beam Induced Deposition Precursor with a Heteroleptic Ligand Set. *Phys. Chem. Chem. Phys.* **2017**, *19* (20), 13264–13271.

(34) Jurczyk, J.; Brewer, C. R.; Hawkins, O. M.; Polyakov, M. N.; Kapusta, C.; McElwee-White, L.; Utke, I. Focused Electron Beam-Induced Deposition and Post-Growth Purification Using the Heteroleptic Ru Complex $(\eta^3\text{-}C_3H_5)Ru(CO)_3Br$. *ACS Appl. Mater. Interfaces* **2019**, *11* (31), 28164–28171.

(35) Rohdenburg, M., Boeckers, H., Brewer, C.R., McElwee-White, L., Swiderek, P., Efficient NH_3-based process to remove chlorine from electron beam deposited ruthenium produced from $(\eta^3$-allyl$)Ru(CO)_3Cl$, *Sci. Rep.* **2020***, 10***,** 10901.

(36) Thorman, R. M.; Jensen, P. A.; Yu, J.-C.; Matsuda, S. J.; McElwee-White, L.; Ingólfsson, O.; Fairbrother, D. H. Electron-Induced Reactions of $Ru(CO)_4I_2$: Gas Phase, Surface, and Electron Beam-Induced Deposition. *J. Phys. Chem. C* **2020**, *124* (19), 10593–10604.

(37) Nguyen, C. T.; Yoon, J.; Khan, R.; Shong, B.; Lee, H.-B.-R. Thermal Atomic Layer Deposition of Metallic Ru Using H_2O as a Reactant. *Appl. Surf. Sci.* **2019**, *488* (March), 896–902.

(38) Madey, T. E.; Faradzhev, N. S.; Yakshinskiy, B. V; Edwards, N. V. Surface Phenomena Related to Mirror Degradation in Extreme Ultraviolet (EUV) Lithography. *Appl. Surf. Sci.* **2006**, *253* (4), 1691–1708.

(39) Warneke, Z.; Rohdenburg, M.; Warneke, J.; Kopyra, J.; Swiderek, P. Electron-Driven and Thermal Chemistry during Water-Assisted Purification of Platinum Nanomaterials Generated by Electron Beam Induced Deposition. *Beilstein J. Nanotechnol.* **2018**, *9*, 77–90.

(40) Winkler, R.; Szkudlarek, A.; Fowlkes, J. D.; Rack, P. D.; Utke, I.; Plank, H. Toward Ultraflat Surface Morphologies During Focused Electron Beam Induced Nanosynthesis: Disruption Origins and Compensation. *ACS Appl. Mater. Interfaces* **2015**, *7* (5), 3289–3297.

(41) *Surface Analysis by Auger and X-Ray Photoelectron Spectroscopy*; Briggs, D., Grant, J. T., Eds.; SurfaceSpectra, 2003.

(42) Schmied, R.; Fowlkes, J. D.; Winkler, R.; Rack, P. D.; Plank, H. Fundamental Edge Broadening Effects during Focused Electron Beam Induced Nanosynthesis. *Beilstein J. Nanotechnol.* **2015**, *6*, 462–471.

(43) Schwalb, C.H.; Grimm, C.; Baranowski, M.; Sachser, R.; Porrati, F.; Reith, H.; Das, P.; Müller, J.; Völklein, F.; Kaya, A.; Huth, M. A Tunable Strain Sensor Using Nanogranular Metals. *Sensors* **2010**, *10*, 9847-9856.

(44) Plank, H.; Kothleitner, G.; Hofer, F.; Michelitsch, S. G.; Gspan, C.; Hohenau, A.; Krenn, J. Optimization of Postgrowth Electron-Beam Curing for Focused Electron-Beam-Induced Pt Deposits. *J. Vac. Sci. Technol., B* **2011**, *29 (051801)*, 1−7.

(45) Plank, H.; Haber, T.; Gspan, C.; Kothleitner, G.; Hofer, F. Chemical Tuning of Ptc Nanostructures Fabricated via Focused Electron Beam Induced Deposition. *Nanotechnology* **2013**, *24 (1753605)*, 1−8.

(46) Plank, H.; Gspan, C.; Dienstleder, M.; Kothleitner, G.; Hofer, F. The Influence of Beam Defocus on Volume Growth Rates for Electron Beam Induced Platinum Deposition. *Nanotechnology* **2008**, *19 (485302)*, 1−9.

(47) NIST Mass Spec Data Center. Mass Spectra. In NIST Chemistry WebBook, NIST Standard Reference Database Number 69; Linstrom, P. J.; Mallard, W. G., Eds.; National Institute of Standards and Technology: Gaithersburg MD, U.S.A., **2020**.

(48) Kim, Y.-K., Irikura, K.K., Rudd, M.E., Ali, M.A., Stone, P.M., Chang, J., Coursey, J.S., Dragoset, R.A., Kishore, A.R., Olsen, K.J., Sansonetti, A.M., Wiersma, G.G., Zucker, D.S. Electron-Impact Cross Sections for Ionization and Excitation Database, NIST Standard Reference Database 107, http://physics.nist.gov/ionxsec, (accessed 20 September 2019).

(49) Spilners, I. J.; Larson, J. G. Mass Spectra of Alkylferrocenes and Biferrocenyls. *Org. Mass Spectrom.* **1970**, *3* (7), 915–924.

(50) Wnuk, J. D.; Gorham, J. M.; Rosenberg, S. G.; van Dorp, W. F.; Madey, T. E.; Hagen, C. W.; Fairbrother, D. H. Electron Induced Surface Reactions of the Organometallic Precursor Trimethyl(Methylcyclopentadienyl)Platinum(IV). *J. Phys. Chem. C* **2009**, *113* (6), 2487–2496.

(51) Engmann, S.; Stano, M.; Matejčík, Š.; Ingólfsson, O. Gas Phase Low Energy Electron Induced Decomposition of the Focused Electron Beam Induced Deposition (FEBID) Precursor Trimethyl (Methylcyclopentadienyl) Platinum(Iv) ($MeCpPtMe_3$). *Phys. Chem. Chem. Phys.* **2012**, *14* (42), 14611.

(52) Begun, G. M.; Compton, R. N. Electron Impact Ionization Studies of Ferrocene, Cobaltocene, Nickelocene, and Magnesocene. *J. Chem. Phys.* **1973**, *58* (6), 2271–2280.

(53) Thorman, R. M.; Unlu, I.; Johnson, K.; Bjornsson, R.; McElwee-White, L.; Fairbrother, D. H.; Ingólfsson, O. Low Energy Electron-Induced Decomposition of (η^5-Cp)$Fe(CO)_2Mn(CO)_5$, a Potential Bimetallic Precursor for Focused Electron Beam Induced Deposition of Alloy Structures. *Phys. Chem. Chem. Phys.* **2018**, *20* (8), 5644–5656.

(54) Corderman, R. R.; Beauchamp, J. L. Negative Ion Chemistry of (η^5-Cyclopentadienyl)Dicarbonylcobalt in the Gas Phase by Ion Cyclotron Resonance

Spectroscopy. The π-Acceptor Ability of Phosphorus Trifluoride Compared to Carbon Monoxide. *Inorg. Chem.* **1977**, *16* (12), 3135–3139.

(55) Warneke, J.; Wang, Z.; Swiderek, P.; Bredehöft, J. H. Electron-Induced Hydration of an Alkene: Alternative Reaction Pathways. *Angew. Chemie Int. Ed.* **2015**, *54* (14), 4397–4400.

(56) Oxgaard, J.; Goddard, W. A. Mechanism of Ru(II)-Catalyzed Olefin Insertion and C−H Activation from Quantum Chemical Studies. *J. Am. Chem. Soc.* **2004**, *126* (2), 442–443.

(57) Liu, N.; Guo, L.; Cao, Z.; Li, W.; Zheng, X.; Shi, Y.; Guo, J.; Xi, Y. Mechanisms of the Water–Gas Shift Reaction Catalyzed by Ruthenium Carbonyl Complexes. *J. Phys. Chem. A* **2016**, *120* (15), 2408–2419.

(58) Zhang, Y.; Zuo, C.; Li, C.; Guo, X.; Zhang, S. Carbonyl Ruthenium Catalysts for the Low-Temperature Water–Gas Shift Reaction with Ionic Liquids as Support Structure Controllers. *Green Chem.* **2016**, *18* (17), 4704–4713.

(59) Garrett, B. C.; Dixon, D. A.; Camaioni, D. M.; Chipman, D. M.; Johnson, M. A.; Jonah, C. D.; Kimmel, G. A.; Miller, J. H.; Rescigno, T. N.; Rossky, P. J.; Xantheas; S. S.; Colson, S. D.; Laufer, A. H.; Ray, D.; Barbara, P. F.; Bartels, D. M.; Becker, K. H.; Bowen, K. H.; Bradforth, S. E.; Carmichael, I.; Coe, J. V.; Corrales, L. R.; Cowin, J. P.; Dupuis, M.; Eisenthal, K. B.; Franz, J. A.; Gutowski, M. S.; Jordan, K. D.; Kay, B. D.; LaVerne, J. A.; Lymar, S. V.; Madey, T. E.; McCurdy, C. W.; Meisel, D.; Mukamel, S.; Nilsson, A. R.; Orlando, T. M.; Petrik, N. G.; Pimblott, S. M.; Rustad, J. R.; Schenter, G. K.; Singer, S. J.; Tokmakoff, A.; Wang, L.-S.; Zwier, T. S. Role of Water in Electron-Initiated Processes and Radical Chemistry: Issues and Scientific Advances. *Chem. Rev.* **2005**, *105* (1), 355–390.

(60) Maitlis, P. M. Tilden Lecture. η^5-Cyclopentadienyl and η^6-Arene as Protecting Ligands towards Platinum Metal Complexes. *Chem. Soc. Rev.* **1981**, *10* (1), 1.

(61) Pagliaro, M.; Campestrini, S.; Ciriminna, R. Ru-Based Oxidation Catalysis. *Chem. Soc. Rev.* **2005**, *34* (10), 837–845.

(62) Lepage, M.; Michaud, M.; Sanche, L. Low Energy Electron Total Scattering Cross Section for the Production of CO within Condensed Methanol. *J. Chem. Phys.* **1997**, *107* (9), 3478–3484.

(63) *CRC Handbook of Chemistry and Physics: A Ready-Reference Book of Chemical and Physical Data*, 77th ed.; Lide, D. R., Frederikse,H. P. R., Eds.; CRC Press: Boca Raton, FL, 1996.

(64) Lewis, B. B.; Stanford, M. G.; Fowlkes, J. D.; Lester, K.; Plank, H.; Rack, P. D. Electron-Stimulated Purification of Platinum Nanostructures Grown via Focused Electron Beam Induced Deposition. *Beilstein J. Nanotechnol.* **2015**, *6* (1), 907–918.

(65) Fowlkes, J. D.; Geier, B.; Lewis, B. B.; Rack, P. D.; Stanford, M. G.; Winkler, R.; Plank, H. Electron Nanoprobe Induced Oxidation: A Simulation of Direct-Write Purification. *Phys. Chem. Chem. Phys.* **2015**, *17* (28), 18294–18304.

TOC Graphic

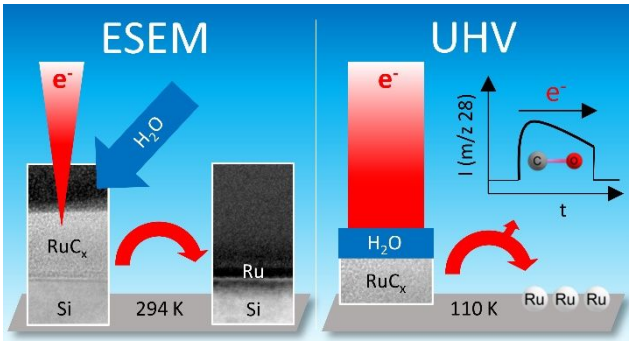
ESEM
UHV
e-
H2O
RuCx
Si
294 K
Ru
Si
e-
H2O
RuCx
110 K
Ru Ru Ru
e-
I (m/z 28)
t
C
O

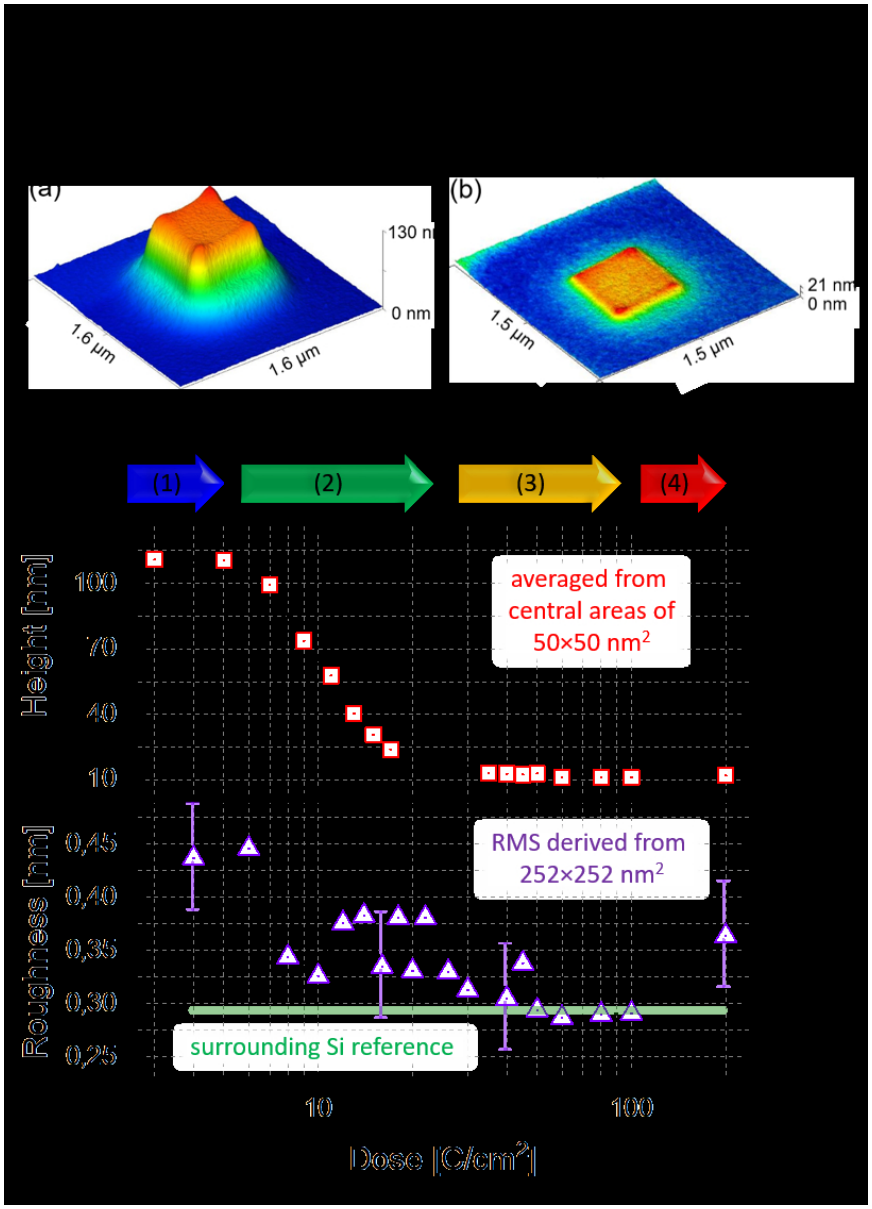

Figure 2. (a) and (b) show 3D AFM height images of a Ru based FEBID deposit before and after a 100 C/cm^2 purification, respectively. While vertical scaling is identical for direct comparison, colors were adjusted to visualize relevant surface details and in particular the crack-free shape fidelity. (c) and (d) show the dose dependent evolution of deposit heights and RMS surface roughness, respectively. Both quantitites are derived from central deposit areas as specified within the graphs. Note the logarithmic abscissa (dose) to reveal the ealy stage behavior. For clarity, only four error bars are shown in (d). Discussion and interpretation can be found in the main text.

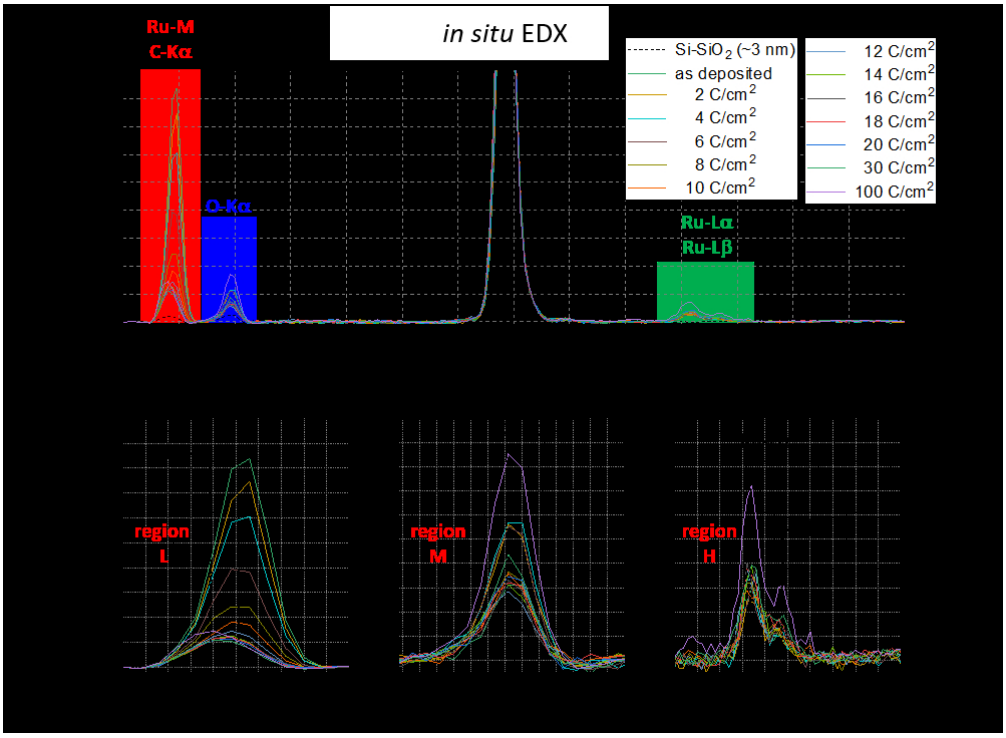

Figure 3. (a) *in situ* EDX spectra obtained after initial fabrication and different purification doses (see legend) without breaking the vacuum to exclude reactions with gases from the ambient. The shaded regions indicate characteristic peaks of different elements, which are shown in more detail in (b), (c) and (d), further denoted as region L, M and H, respectively.

168x123mm (150 x 150 DPI)

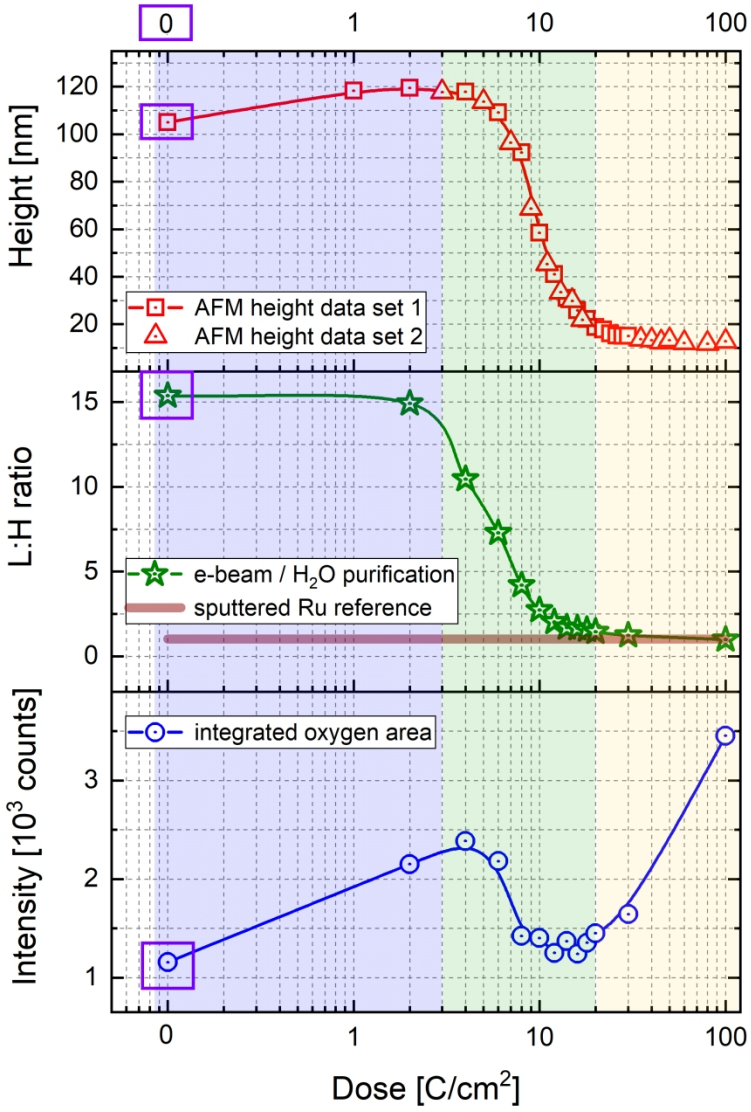

Figure 4. Dose dependent evolution of the deposit height for two data sets from different experiment measured by AFM (red squares / triangles, top panel), L:H intensity ratio as a measure for carbon removal (green stars, central panel) together with the Ru reference value from sputter-cleaned Ru samples (purple horizontal line, central panel), and oxygen intensity (blue circles, bottom panel). Note the logarithmic abscissa for the dose and that as-deposited values at the very left are emphasized by purple frames to visualize the evolution.

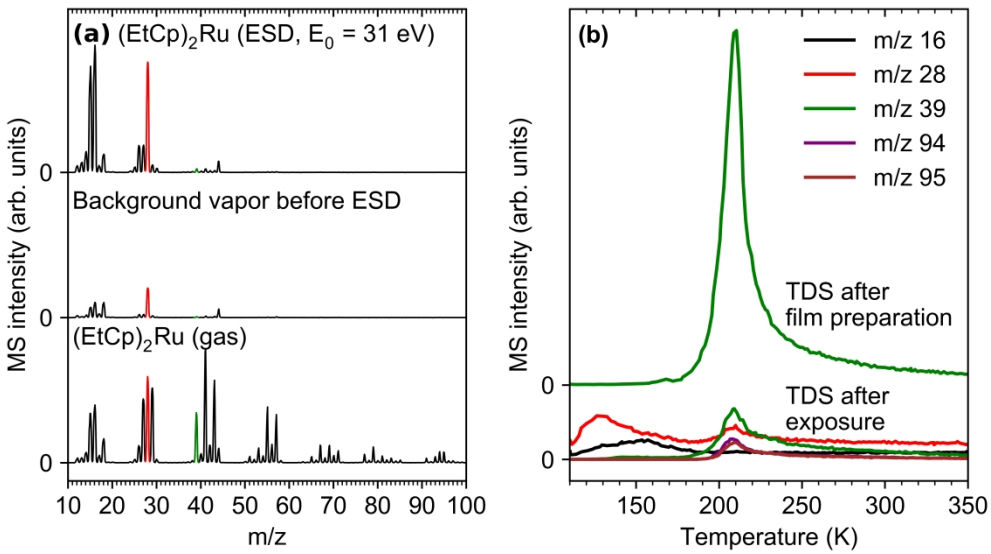

Figure 5. Mass spectra recorded (a) during electron exposure of 40 mC/cm² at E_0 = 31 eV of an adsorbed layer of $(EtCp)_2Ru$ with thickness of 13-20 ML on a Ta substrate held at 110 K, (b) before the start of irradiation, and (c) during dosing of $(EtCp)_2Ru$ onto the Ta substrate. (d) TDS experiments performed directly after preparation of the precursor layer and after electron exposure of 40 mC/cm² at E_0 = 31 eV. After the temperature ramp terminated at 350 K, the temperature was rapidly increased to 450 K where it was held for 30 s in a final annealing step.

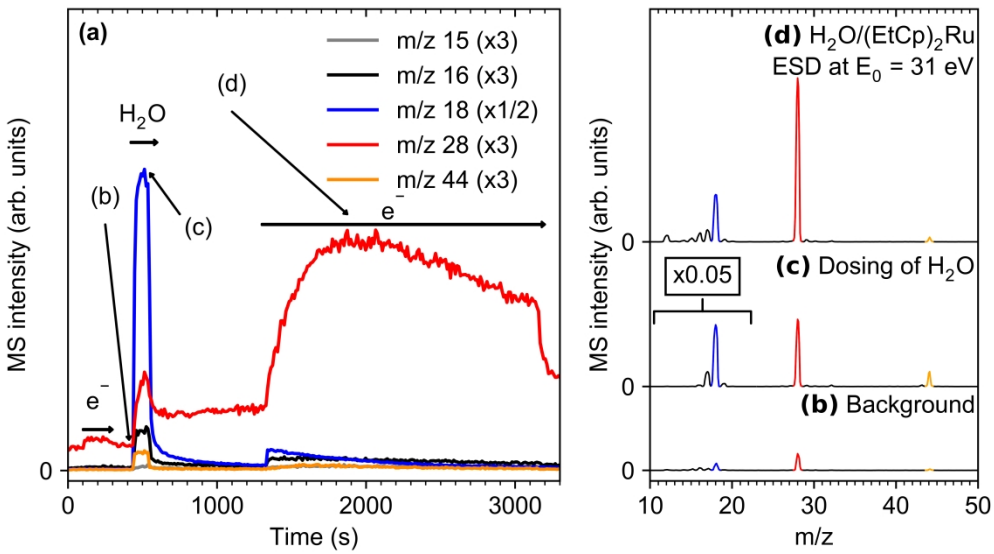

Figure 6. (a) Isothermal and electron-stimulated desorption spectrum (ISD and ESD) extracted from a sequence of rapid mass scans recorded during a water-assisted purification model experiment on a $(EtCp)_2Ru$ deposit. The deposit was produced beforehand by irradiating a 13-20 ML film of $(EtCp)_2Ru$ at E_0 = 31 eV until the production of volatile products in ESD had ceased (40 mC/cm²). The deposit was annealed to 450 K for 30 s and cooled back to 110 K before acquiring the data shown. A short electron exposure (100-300 s, 31 eV, 2 mC/cm², marked by e^-) was applied at the beginning of the purification experiment to verify that no further ESD occurred. A total amount of 40-80 ML H_2O was then dosed onto the deposit held at 110 K (400-600 s, marked by H_2O). Finally, a further electron exposure (1300-3150 s, 31 eV, 20 mC/cm², marked by e^-) was performed at the same temperature. Representative mass scans show the gas phase composition (b) immediately before dosing H_2O, (c) during H_2O dosing, and (d) at the maximum of CO evolution (m/z 28) during the final electron exposure step. The m/z 10-20 range in (b) is scaled to 0.05% of its actual intensity to enhance the visibility of less intense signals.

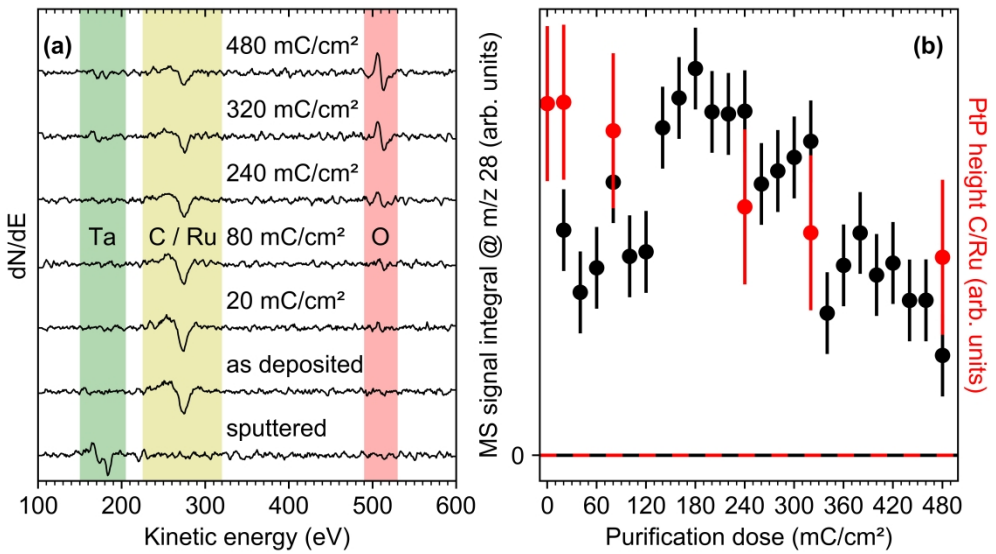

Figure 7. (a) Derivative AES of the freshly sputtered Ta sheet, an as-deposited $(EtCp)_2Ru$ layer (after 40 mC/cm² at E_0 = 31 eV), and the same layer after selected purification exposures of up to 480 mC/cm² in total. Overall, 24 purification cycles were carried out, each involving electron exposure of 20 mC/cm² at E_0 = 31 eV in the presence of 20-40 ML or 40-80 ML H_2O condensed on the deposit and followed by annealing to 450 K. (b) Plot of the total Peak-to-Peak (PtP) height of the C/Ru AES signal (red) and the total IDS CO signal (as integrated desorption signal on m/z 28, black) against purification exposure. Note that the third and the sixth purification cycle applied only 20-40 ML H_2O to the deposit whereas the remaining cycles were carried out with 40-80 ML H_2O.